ENERGY LABORATORY

MASSACHUSETTS INSTITUTE
OF TECHNOLOGY

FUNDAMENTAL ASPECTS OF COAL-WATER FUEL DROPLET COMBUSTION AND SECONDARY ATOMIZATION OF COAL-WATER MIXTURES

FINAL REPORT, Volume I

by

S.W. Kang, A.F. Sarofim
J.D. Teare and J.M. Beér

MIT-EL 87-002 February 1987

DOE/PC/70268-F1

FUNDAMENTAL ASPECTS OF

COAL-WATER FUEL DROPLET COMBUSTION

and

SECONDARY ATOMIZATION OF COAL-WATER MIXTURES

FINAL REPORT

Prof. Adel F. Sarofim
Prof. János M. Beér

Principal Investigators

Volume I

Massachusetts Institute of Technology
Energy Laboratory
and
Department of Chemical Engineering
Cambridge, Massachusetts 02139

Date Prepared - November 1986

Prepared for

United States Department of Energy
Pittsburgh Energy Technology Center
Fossil Energy Program

Under Grant No. DE-FG22 - 84PC70268

DISCLAIMERS

FOREWORD

Grant Number DE-FG22-84PC70268 covered research carried out at the Massachusetts Institute of Technology during the period October 1984 - September 1986. All of this research related to combustion of coal-water fuels, but the workscope covered two entirely separate tasks which involved experimental work in three different facilities at MIT.

The Task 1 investigations dealt with Fundamental Aspects of Coal-Water Fuel Droplet Combustion, and the experiments were carried out in Laminar Flow Reactors. The Technical Monitor at the DOE Pittsburgh Energy Technology Center for this portion of the work was Dr. James D. Hickerson.

The Task 2 research was on Secondary Atomization of Coal-Water Mixtures, and this involved measurements on a Spray Test Rig to characterize spray atomization quality of fuels with various treatments, followed by combustion tests in a 1-3 MW_{th} Combustion Research Facility. The Spray Test Rig was also used to characterize the nozzle used in the Task 1 work. The Task 2 Technical Monitor was Mr. Charles McCann, who was also the Project Manager for the Grant.

Because of the disparate nature of these separate-but-related Tasks, this Final Report is issued in two volumes; Volume I covers the Fundamental Aspects and Volume II deals with Secondary Atomization.

RESEARCH TEAM

Principal Investigators

Professor J.M. Beér
Professor A.F. Sarofim

Research Group	Tasks
Prof. J.M. Beér	1, 2
Dr. D. Froelich	1
Mr. S.W. Kang	1, 2
Mr. S.G. Kang	1
Prof. A.F. Sarofim	1, 2
Dr. S. Srinivasachar	1
Dr. J.D. Teare	1, 2
Mr. L.D. Timothy	1
Dr. M.A. Toqan	2
Dr. P.M. Walsh	2
Dr. T.U. Yu	2

Reports Prepared by:

Volume I	Volume II
S.W. Kang A.F. Sarofim J.D. Teare J.M. Beér	T.U. Yu S.W. Kang J.M. Beér J.D. Teare M.A. Toqan A.F. Sarofim

ACKNOWLEDGEMENTS

The authors would like to acknowledge the help of Dr. S.C. Rah in the initial experiments in which the droplet generator was coupled to a Laminar Flow Reactor.

They are also grateful to Ms. C. Turnburke for her care and patience in the preparation of this report.

ABSTRACT

This Final Report is issued in two volumes, covering research into the combustion of coal-water fuels (CWF). Two separate but related tasks are discussed; the present report, Volume I, contains results obtained under Task 1 - "Fundamental Aspects of Coal-Water Fuel Droplet Combustion." Volume II describes the work of Task 2 - "Secondary Atomization of Coal Water Mixtures," which included experimental measurements in a Spray Test Facility and in the 1-3 MW_{th} Combustion Research Facility.

The processes of devolatilization and char combustion were studied in a laminar flow reactor (LFR) by two experimental procedures. In the first of these, a CWF droplet generator was developed and used to feed CWF droplets directly into the LFR. The CWF droplet generator, which consists of a twin-fluid, internally-mixed atomizer and a series of skimmers to reduce the feed rate of droplets into the LFR, is capable of producing CWF droplets in the size range of 5-500 micrometers at feed rates of less than 3 mg/sec.

In the second parallel study, solid samples withdrawn from a CWF spray flame, close to the atomizing nozzle, were size graded and fed into the LFR in low particle concentrations. Their combustion history in the LFR was determined by monitoring the intensity of radiation emitted by individual particles during combustion (by two-color pyrometry) and by the use of high speed cinematography.

The study has established the importance of rotation induced by the volatile evolution on the break up of coal-aggregates and the release of ash particles. Particle rotation during devolatilization and char combustion generates centrifugal forces at the particle surface which can promote the separation of both weakly adhering char fragments and ash particles.

The results show that there is a competition between centrifugal forces which favors the break up of coal-aggregates and adhesive forces between coal particles during the plastic stage of coal pyrolysis. Based upon the theoretical model of agglomeration, the adhesive force on the process of coalescence of coal particles is strongly dependent on the duration of plasticity of the particles. It is also found that rapid heating reduces the tendency of coal particles to form aggregates during the CWF droplet evaporation. Therefore, whether particles burn individually or as aggregates can be influenced by the temperature history of the CWF particle and hence by burner design.

TABLE OF CONTENTS

CHAPTER 1. INTRODUCTION

1.1. Introduction

The two major applications of coal-water fuel (CWF) are the replacement of petroleum fuels in existing oil-fired boilers [1], and in coal-fired (open cycle) gas turbines [2]. Both of these applications represent relatively novel, developing technologies. Boiler applications are expected in this decade and gas turbine applications in the 1990's. While many of the current problem areas in combustion of CWF are common to both applications, the more immediate concern is clearly focused on the boilers.

Coal beneficiation to the level needed for retrofit of boilers designed for oil (about 2-3% ash) requires fine grinding of the coal (~ 80% < 76 μm) and a maximum of about 30-40 wt % water to be compatible with demands of efficient coal cleaning, favorable rheologic properties of the slurry and a limited increase in waste gas heat losses of the boilers. The water in the CWF engenders operational difficulties in achieving ignition and good flame stability over practical ranges of the turn-down ratio (about 1:3), which sets this fuel apart from pulverized coal and even from high moisture lignite. The ignition difficulty is due mainly to the requirement that all the water in the fuel spray has to be evaporated before the coal can be heated to ignition. The conditions for ignition are more severe than for the combustion of pulverized low rank coals with high moisture content, since for these coals most of the drying occurs in the grinding mill prior

to injection of the fuel into the combustion chamber. Another factor affecting ignition is agglomeration of the residue of the CWF droplets. This causes a shift to larger effective particle size and loss of the potential benefits of using very fine coal particles.

Effective particle size is very important from another aspect of retrofitting an oil-fired boiler, which is designed to operate with residence times much shorter than would be desirable in a unit designed for pulverized coal-firing. Burnout of the residual char from the CWF particles cannot be achieved unless the particle size is maintained sufficiently small.

During CWF droplet combustion, there is a tendency for the coal particles to agglomerate within droplets. Hence, the resulting coal particle size distribution (p.s.d.) is determined by the size distribution of the atomized CWF droplet rather than by the original particle size of the coal. When there are multiple particles within a single droplet, interfacial forces come into play during the drying process, so that the particles tend to agglomerate. When a coal-water fuel is sprayed into a furnace, the drying process precedes and overlaps the early stage of pyrolysis, during which swelling of the coal particles is likely to occur. Most of the coal-water fuels currently under production use high-volatile coals in order to aid in the ignition process, but such coals in general have a high swelling index. After the agglomerate reaches a temperature around 400°C, tar-like hydrocarbons are released, and the particles become more effectively bonded. The agglomerate

then enters the plastic deformation stage, and volatiles are evolved through devolatilization pores. Examinations of the behavior of single droplets of coal-oil mixtures during combustion [3] have shown that the strength of the agglomerate is dependent upon coal rank, with swelling coals fusing as described above, while non-swelling coals form loosely sintered aggregates which readily fall apart during combustion. Given that the burnout time for a particle of diameter d is proportional to d^n, with $1 < n < 2$, it is important that the conditions under which aggregates form and survive be well-understood. This is especially so for applications which use micronized coal in the slurry, as the investment in producing the ultra-fine grind is virtually wasted if agglomeration determines the p.s.d.

Another area of concern in retrofit applications is the behavior of the ash from the coal, since even after beneficiation the ash burden is considerably higher than that in most fuel oils. Factors which influence this ash behavior include the ash composition and the temperature-time environment which an ash particle encounters as it is swept through the furnace. Once again, however, it is the ash particle size which determines whether the particle will follow the gas streamlines as it passes through the convective sections, with larger particles being subject to impaction and possible entrapment within a surface deposit.

Thus from the viewpoints of ignition/stability, of good carbon burnout, and of minimization of deposit formation, the

behavior of the coal particles during combustion is seen to be of crucial importance.

1.2. Objective of Investigation

During CWF droplet combustion, the water evaporates leaving a loose agglomerate of the coal particles, and the coal particle agglomerates will be heated further and fuse together as they pass through the coal softening temperatures. The strength of the bonds between particles will be greatest for high-volatile swelling coals, and relatively weak for the non-swelling lignites and anthracites. The coal agglomerate will then ignite and devolatilize. The residual char will burn out at a rate that will be strongly dependent on its particle size, as well as on process conditions of temperature and oxygen partial pressure, and on coal-dependent parameters such as intrinsic coal reactivity, internal surface area, and pore size distribution. The loosely aggregated char particles will break up during burnout, and their burnout times will be correspondingly short. The particle break-up will also influence the size of the ash product. The residual ash is produced by the coalescence of the fused mineral inclusions within the char which are brought together as the burning char surface recedes. Some smaller ash particles are also produced when these fused mineral inclusions are released during burnout.

The objective of this study is to determine the factors that govern ash particle size distribution (p.s.d.), and examine conditions under which coal-aggregates, produced during the CWF droplet evaporation, can be induced to break up.

CHAPTER 2. EXPERIMENTAL INVESTIGATION

The processes of particle agglomeration, particle rotation, and fragmentation during devolatilization and char combustion were studied in a laminar flow reactor (LFR) by two experimental procedures. In the first of these, a new CWF droplet generator was developed and was used to feed CWF droplets directly into the LFR. The droplet generator, which consists of a twin fluid atomizer and a series of skimmers to reduce the feed rate of droplets into the LFR, is capable of producing CWF droplets in the size range of 5-500 μm and feed rates less than 3 mg/s.

In the second, parallel study, solid samples withdrawn from a coal-water fuel (CWF) spray flame, close to the atomizing nozzle, were size graded and fed into the LFR in low particle concentrations. Their combustion history in the LFR was determined by monitoring the intensity of radiation emitted by individual particles during combustion (by two-color pyrometry) and by the use of high speed cinematography.

The experimental apparatus for a CWF droplet injection will be discussed in Section 2.1, and that for a CWF agglomerate (solid sample) injection will be discussed in Section 2.2.

2.1. Experimental Apparatus for CWF Droplet Injection

The experimental apparatus for CWF droplet injection, schematically shown in Figure 1, consists of a CWF droplet generator, a laminar flow reactor, a feeding probe, a sample

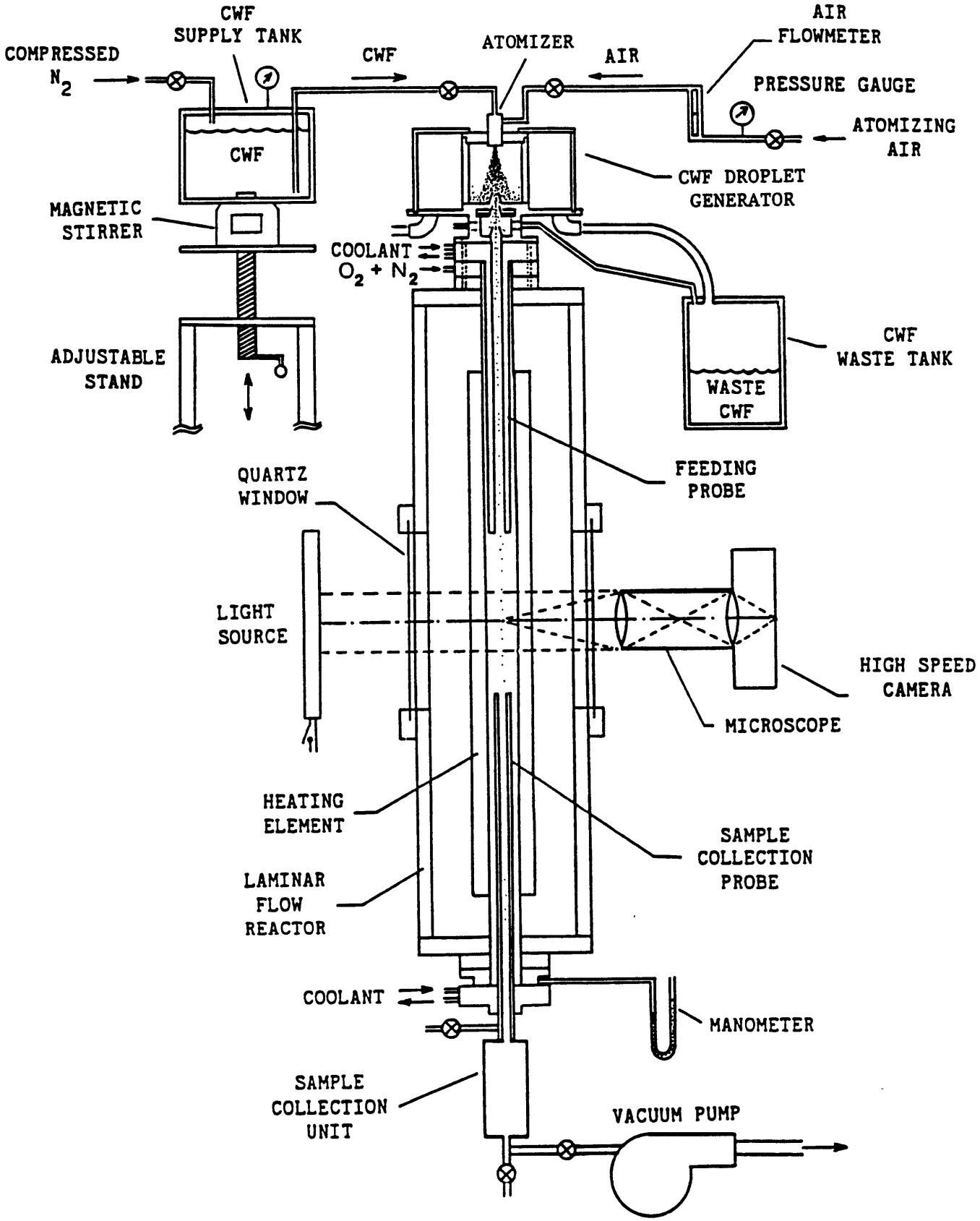

Figure 1. Schematic Diagram of Experimental Apparatus (CWF Droplet Injection)

collection system, a fuel supply tank, a fuel waste tank, and a photographic recording system.

2.1.1. CWF Droplet Generator

The schematic diagram of the CWF droplet generator is shown in Figure 2. It consists of an atomizer, an atomizer adaptor, a 10 cm diameter cylinder with sixteen holes 2 cm in diameter, enclosed in a 25 cm diameter plexiglas tank, a base plate, and three cone-shaped skimmers with different openings. A wide angle CWF spray, generated from the atomizer, was discharged into the cylinder, and then passed through the series of skimmers with progressively larger openings to chop most of the CWF spray. This produced a narrow dilute stream of CWF droplets which was fed directly to the LFR. The remainder of the CWF spray was discharged to a waste fuel collecting tank from the six ports in the CWF droplet generator through flexible vinyl hoses. The range of the opening diameters of the first skimmer was 0.3 cm to 0.6 cm, and that of the second skimmer was 0.4 cm to 0.7 cm, and that of the third skimmer was 0.5 cm to 0.8 cm. The opening sizes of the skimmer used for a particular experiment were chosen based on the desired skimmed CWF flowrate to the laminar flow reactor.

2.1.2. Atomizer

The twin-fluid, internally-mixed, single-exit atomizer was developed to generate a stream of coal-water fuel (CWF) droplets in the size range of 5 to 500 μm. Figure 3 shows the schematic

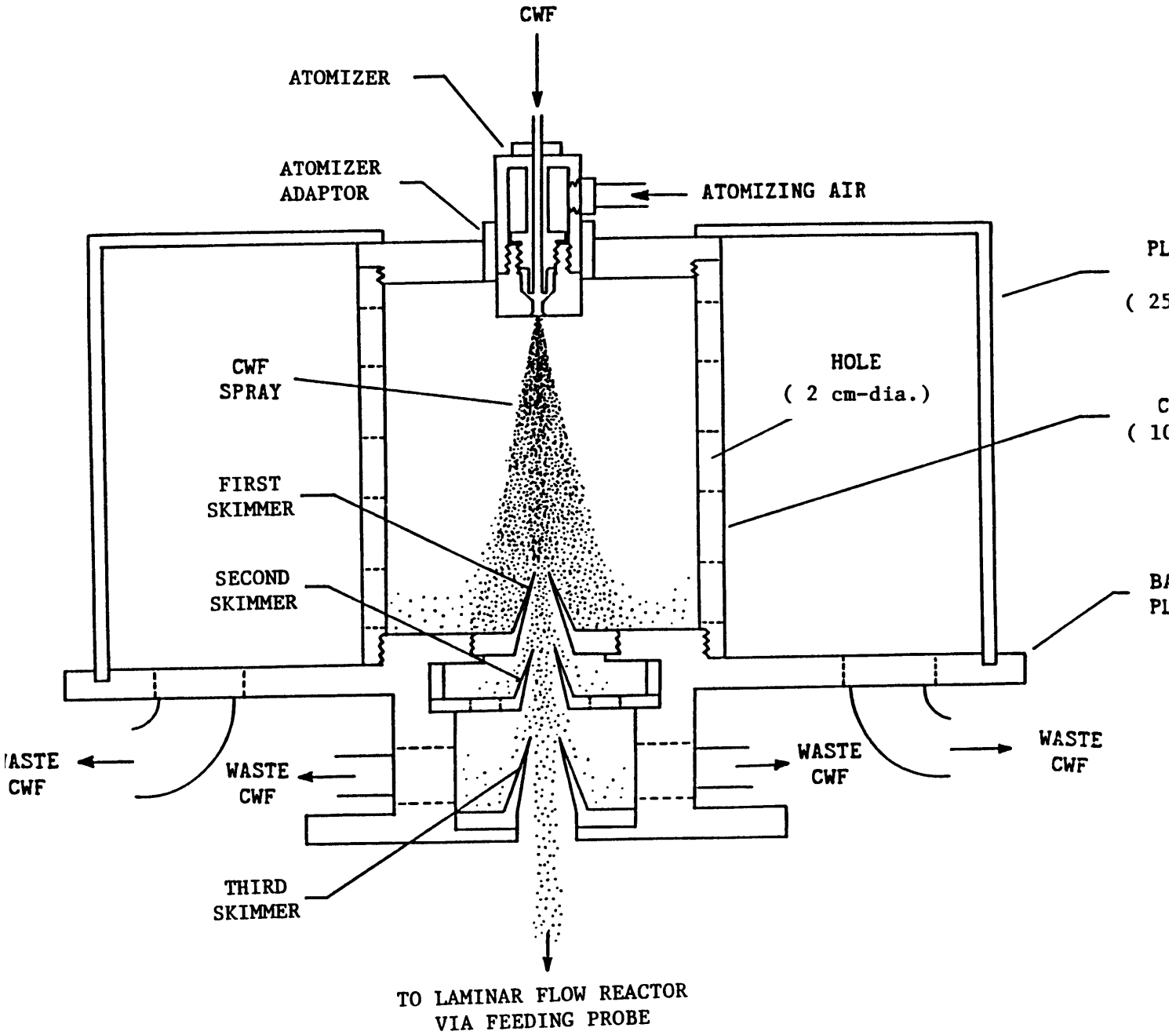

Figure 2. Schematic Diagram of CWF Droplet Generator

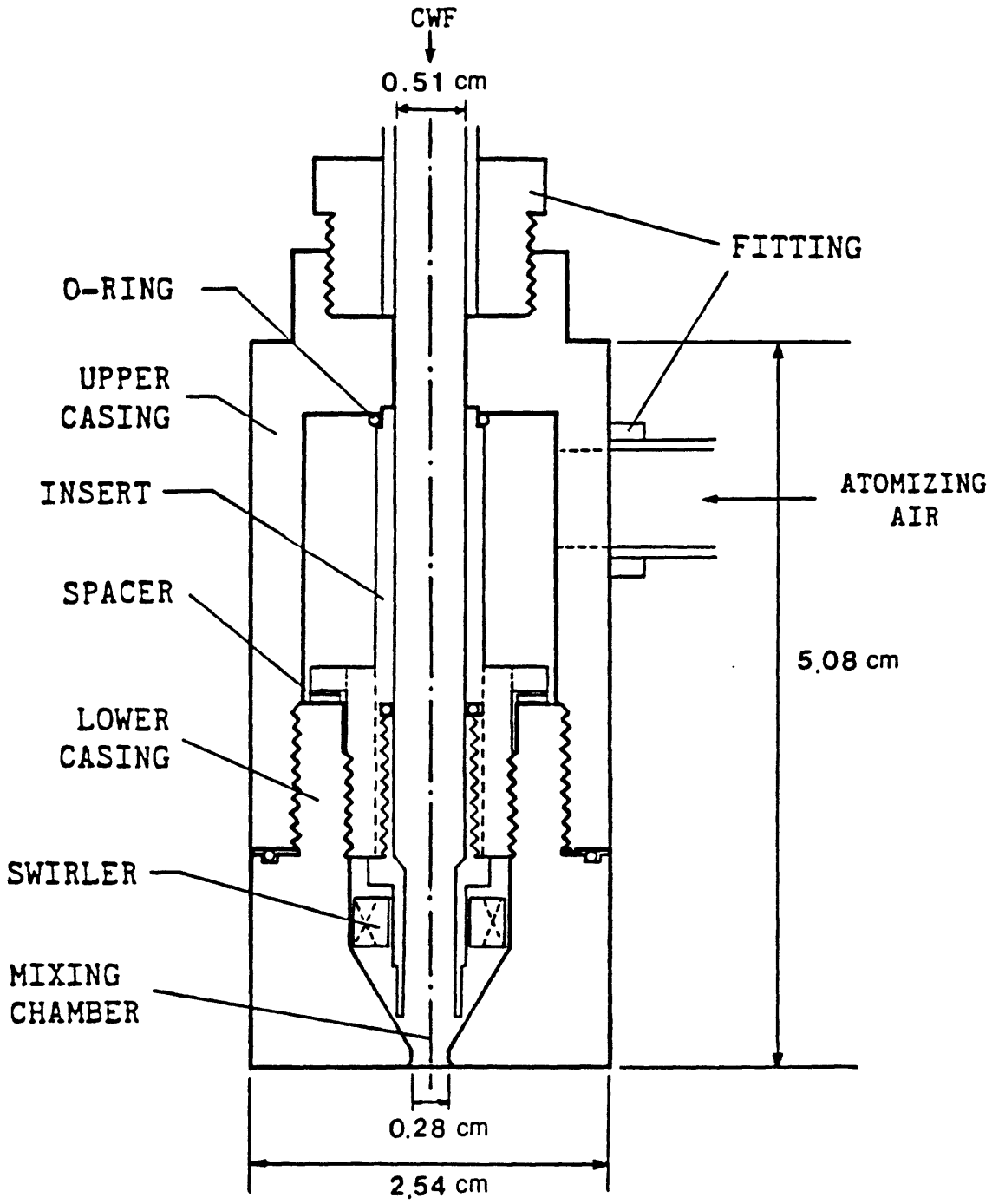

Figure 3. Schematic Diagram of Atomizer

diagram of the atomizer. It consists of an upper casing, a lower casing, an insert, a swirler, a spacer, O-rings, and fittings.

The atomizing air at 15-20 psig was supplied through the air passage of the insert, the swirler, and the mixing chamber. This atomizing air entrained the CWF up to the mixing chamber by syphon action, producing a high atomizing air-to-fuel ratio (AFR) and a fine droplet size (28 μm Mass Mean Diameter). The coal-water fuel (CWF) was supplied from the fuel tank to the nozzle through 0.6 cm ID tubing. To obtain a larger mean droplet size, the CWF flowrate could be increased by supplying the fuel to the nozzle at higher fuel tank pressure (1-5 psig).

The atomizing air and the entrained CWF were mixed internally in the mixing chamber and discharged from a common orifice (0.28 cm diameter) into the skimmers. The swirler in the mixing chamber increased the spray angle. The spacer, which was located between the lower casing and the insert, could adjust the cross-sectional area of the air passage leading to the mixing chamber. By adjusting this cross-sectional area, mean droplet size and particle size distribution of CWF spray could be changed. The three O-rings prevented leakage of the atomizing air, which resulted in oscillation of the CWF spray. The nozzle orifice has a 40° (full angle) external chamfer to increase the spray angle.

The atomizer was tested in a Spray Test Facility which was equipped with a Laser Diffraction Spray Analyzer. The descriptions of the Spray Test Facility and the Laser Diffraction Spray Analyzer and the results of the atomizer test are discussed in Appendix A.

2.1.3. Laminar Flow Reactor

The laminar flow reactor, shown schematically in Figure 4, was manufactured by Astro Industries, Inc. (Santa Barbara, CA). Overall furnace dimensions are 25.4 cm diameter by 111.7 cm length[4].

Two windows, 1.3 cm wide by 30.5 cm long, are located on opposite sides of the furnace and symmetrically centered about the hot zone. The windows are sealed with 0.3 cm thick quartz plates. A port is provided at the center of the hot zone in a plane perpendicular to that of the windows for a Graphite/Boronated Graphite thermocouple (Astro BGT-2). A water-cooled 5.1 cm diameter O-ring seal assembly is provided at each end of the furnace to support a quartz tube that extends the length of the furnace.

The graphite heating element is supported from two power feed-throughs at one end of the furnace. This configuration limits the furnace orientation to a length-wise vertical position. The heating element is located between the quartz tube and the graphite radiation shield. The cavity containing the heating element is continuously flushed with helium (Figure 5), which is introduced via a rotameter through orifices located in the window assembly and vented through a port in the casing at the lower end of the furnace. In the event of an over-pressurization of the casing, a pressure release valve is furnished through a port in the casing at the upper end of the furnace.

Power for the heating element is provided by a 20 kVA power supply consisting of a phase angle fired silicon controlled

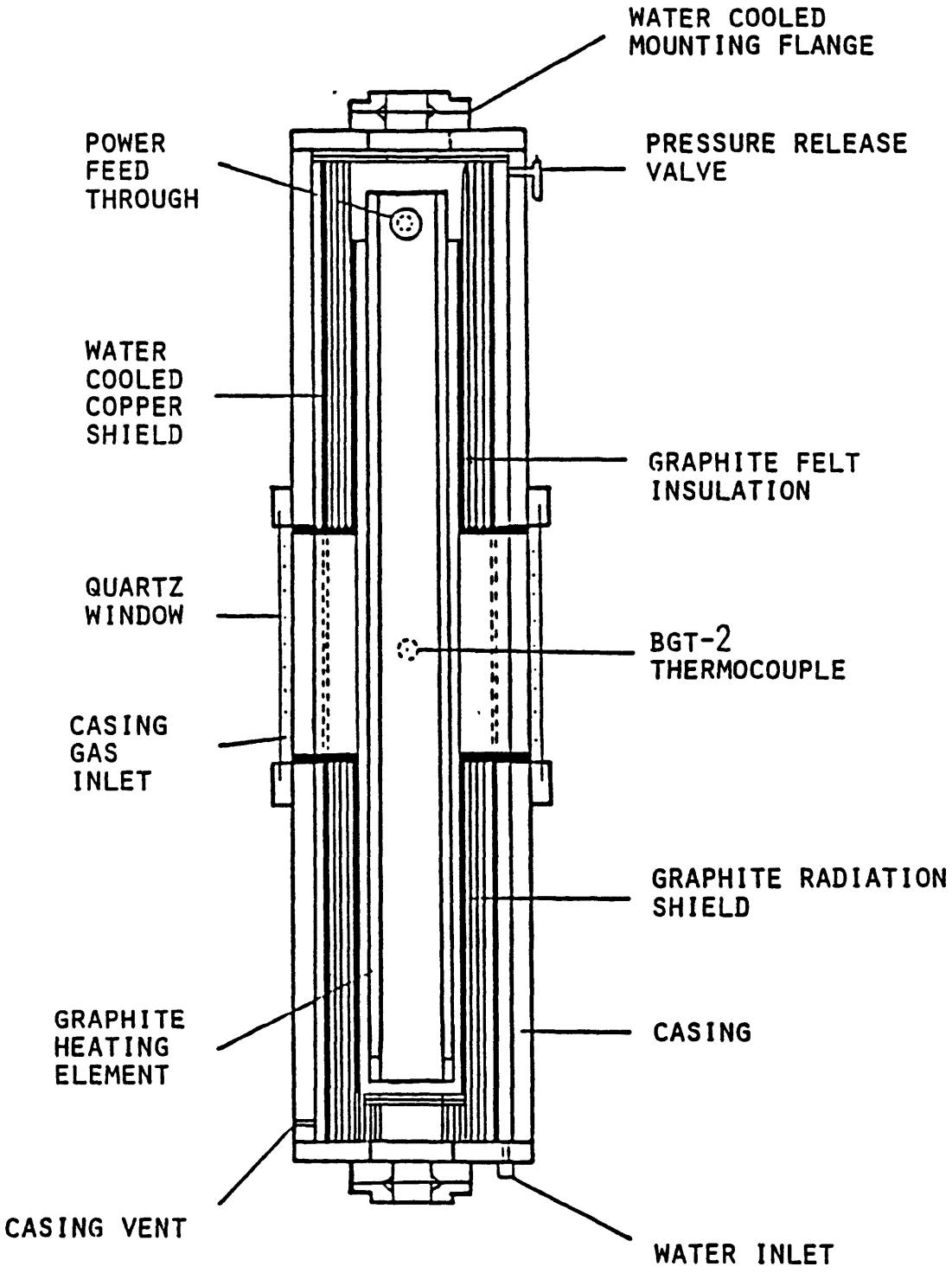

Figure 4. Schematic Diagram of Laminar Flow Reactor

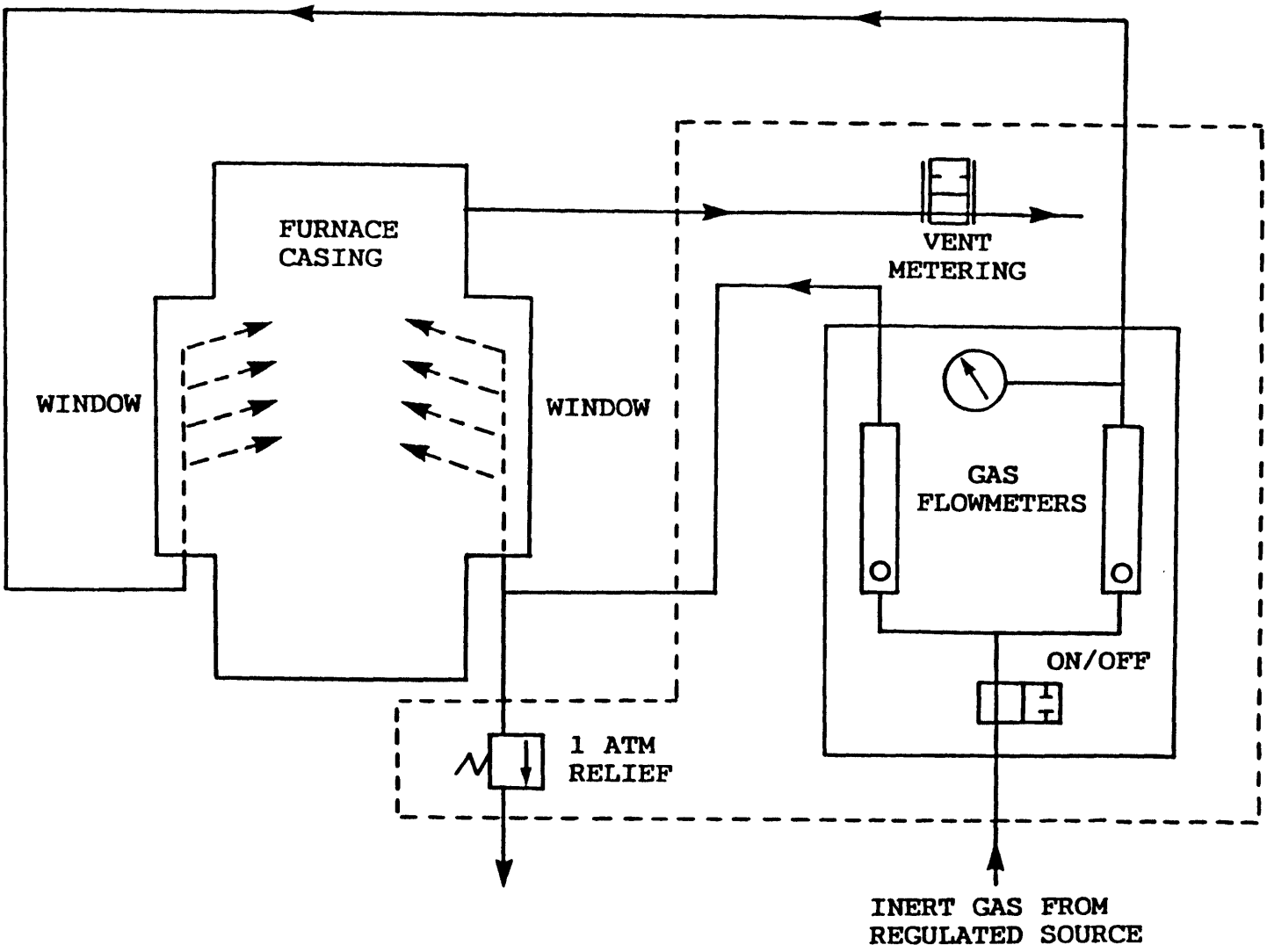

Figure 5. Schematic Diagram of Furnace Casing Gas Flow

rectifier power regulator and a step-down load transformer. Power may be manually adjusted or automatically adjusted by a digital control programmer (Honeywell DCP-7700).

The signal for the programmer is produced by the Graphite/Boronated Graphite thermocouple and transformed to a compatible programmer input by a signal transmitter (Rochester Instrument Systems, Model SC-1304). The BGT-2 thermocouple has an exceptionally high output and sensitivity throughout its entire operating temperature range, providing stable long-time operation to 2,250 K. All designs of this type of thermocouple have appreciable thermal mass and conduction losses along the graphite supporting elements to the water-cooled cold-junction and thus must be calibrated.

The furnace is mounted on an elevating support stand. The position of the furnace may be manually adjusted through a 30 cm vertical displacement. The furnace mounting bracket on the stand slides on hardened and ground shafts with linear ball bushings to provide smooth vibration-free operation.

2.1.4. Feeding Probe

A narrow stream of CWF droplets was fed into the laminar flow reactor through a feeding probe whose inside-diameter may be varied between 0.8 cm and 2.4 cm. The feeding probe was kept cool in the combustion zone by circulating cooling water.

2.1.5. Sample Collection Probe

The water-cooled sample collection probe was connected to the bottom of the furnace. A vacuum pump pulled the exhaust gases and particles through the sample collection probe to a filter which removed the solid particles. The pressure inside the furnace could be changed by adjusting bleed valves between the sample collection filter and the vacuum pump. The pressure inside the furnace was monitored by a water-column manometer. The sample collection filter could be replaced by a cascade impactor to measure ash particle size distribution.

2.1.6. Fuel Supply Tank

The coal-water fuel was supplied from a fuel supply tank to the nozzle. The CWF flowrate could be changed by adjusting the fuel tank pressure. This pressure was controlled by adjusting the air flowrate to the fuel tank. The fuel supply tank was mounted on an adjustable-height stand. The level of CWF in the fuel tank was maintained constant relative to the ground level by adjusting the position of the fuel tank. This provided constant fuel tank pressure during the experiment. A magnetic stirrer was used under the fuel tank to mix the CWF thoroughly.

2.1.7. Photographic Recording System

A high speed cinematographic camera (HYCAM) equipped with a microscope (HEERBRUGG MDG 13) was used for observing and recording the combustion process through the quartz window on the furnace.

The microscope provided magnification of the burning CWF droplets in the range of 0.3 X to 3.7 X. A light source was located opposite the camera to give the background light for the transmission photographic study (Figure 1).

2.2. Experimental Apparatus for CWF Agglomerate Injection

The experimental apparatus for CWF agglomerate (solid-sample) injection, schematically shown in Figure 6, consists of a laminar flow reactor, a solid-sample feeding system, a collection system, a two-color pyrometer, and a photographic recording system.

2.2.1. Laminar Flow Reactor

Figure 7 shows the schematic diagram of the laminar flow reactor[5] (Astro Model 1000A). The furnace has electrically heated graphite elements, the temperature of which is regulated with an automated current controller. In order to protect the graphite heating elements from the oxidizing environment, the elements are isolated from the central combustion zone by an alumina muffle tube. Due to the thermal limitation imposed by the alumina, the maximum operating furnace temperature is 1800 Kelvin. The main gas, a pre-mixed oxygen inert gas, enters at 10^{-4} m^3/s through the top of the furnace where it flows through an alumina honeycomb at the top of the hot zone, an isothermal region of 0.15m. The honeycomb serves as both a flow straightener and preheater, delivering the main gas at the specified furnace temperature with a uniform laminar velocity. The composition of

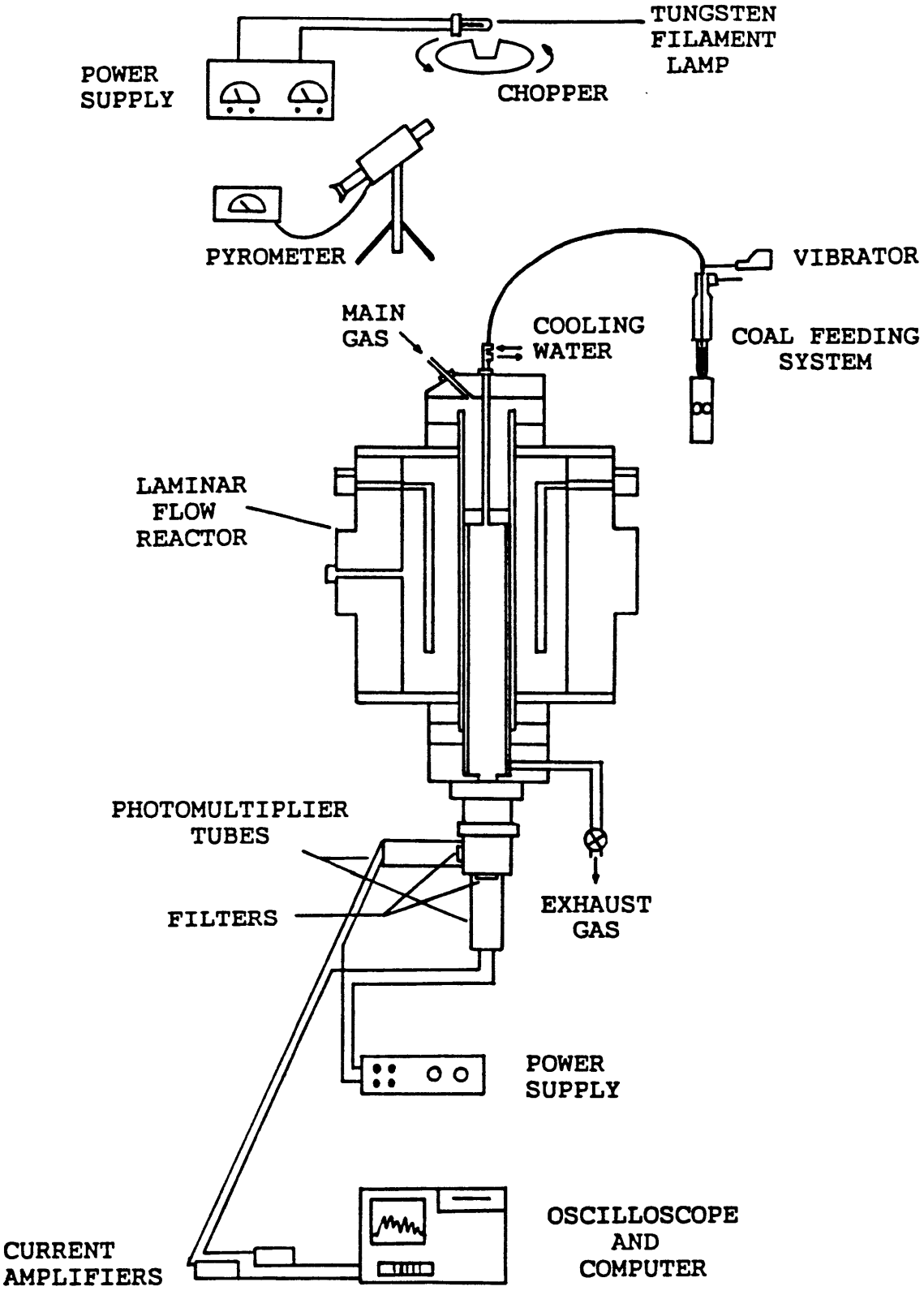

Figure 6. Schematic Diagram of Experimental Apparatus (CWF Agglomerate Injection)

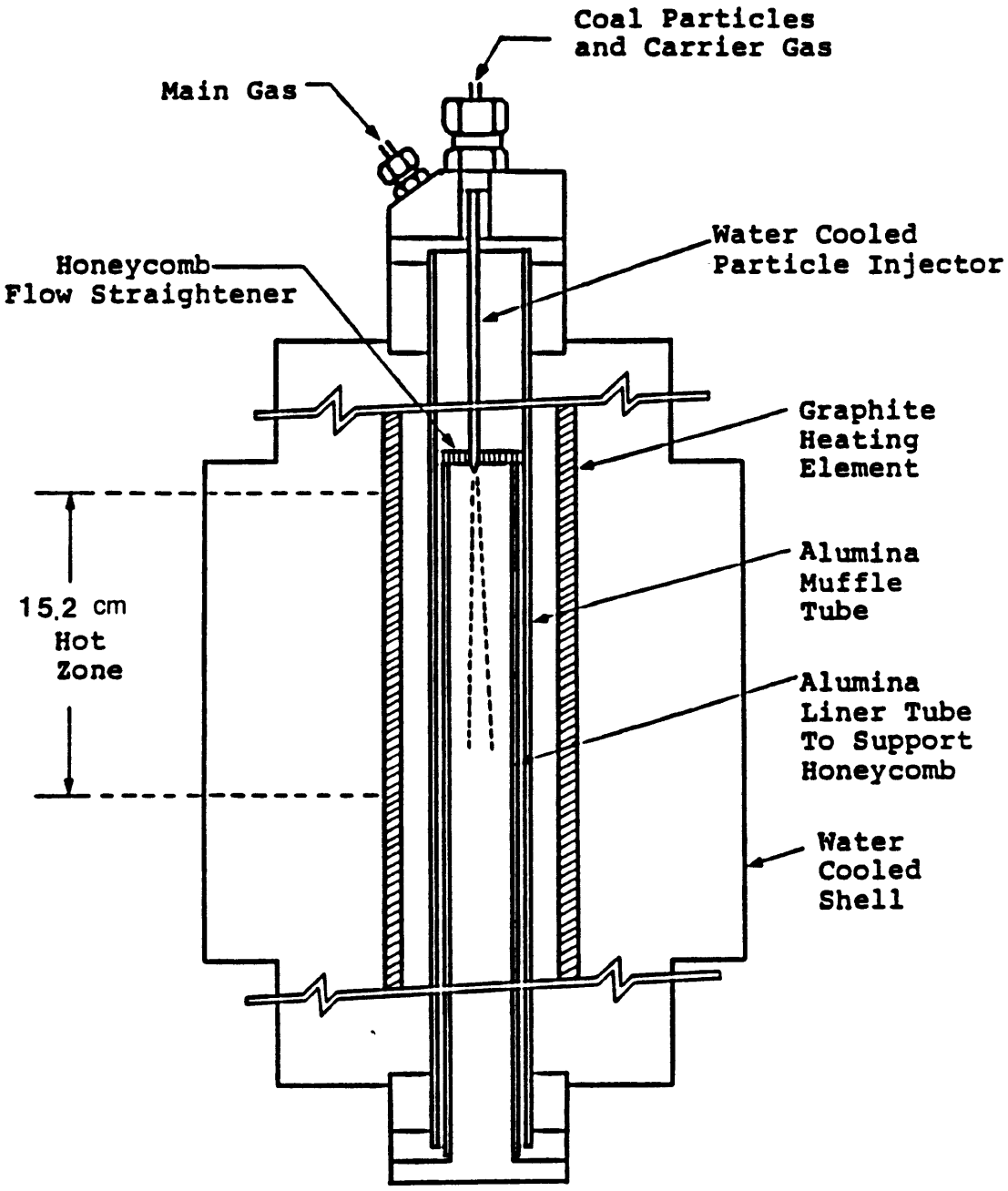

Figure 7. Schematic Diagram of Laminar Flow Reactor

oxygen-nitrogen gas mixture is regulated by dual mass flow controllers. Size-graded CWF agglomerates are fed through a narrow water cooled feeder tube and injected axially into the main gas stream just below the honeycomb. The CWF agglomerates are rapidly heated and combustion begins. Radial dispersion of the particles is minimized by the stable laminar flow field.

2.2.2. Solid-Sample Feeding System

A schematic diagram of the solid-sample feeding system is presented in Figure 8. The CWF agglomerates are entrained by the inert carrier gas, which flows over the surface of the agitated coal bed and into the stationary fine gauge tubing. The gas velocity in the fine gauge tubing is sufficient to keep the particles in suspension. The rate of entrainment is established by the rate at which the coal feed vial is driven towards the stationary fine gauge tubing by the syringe pump. A range of feeding rates from 1.7×10^{-4} grams/s to 1.7×10^{-3} grams/s is obtainable by changing the speed of the syringe pump. For a given syringe setting, a fixed clearance between the top of the coal bed and the fine gauge tube will be established after an initial transient. One to three grams of CWF agglomerates are normally fed per experiment.

2.2.3. Collection Probe

All the combustion products, both gaseous and solid ,are collected at a given height in the furnace by a water-cooled probe

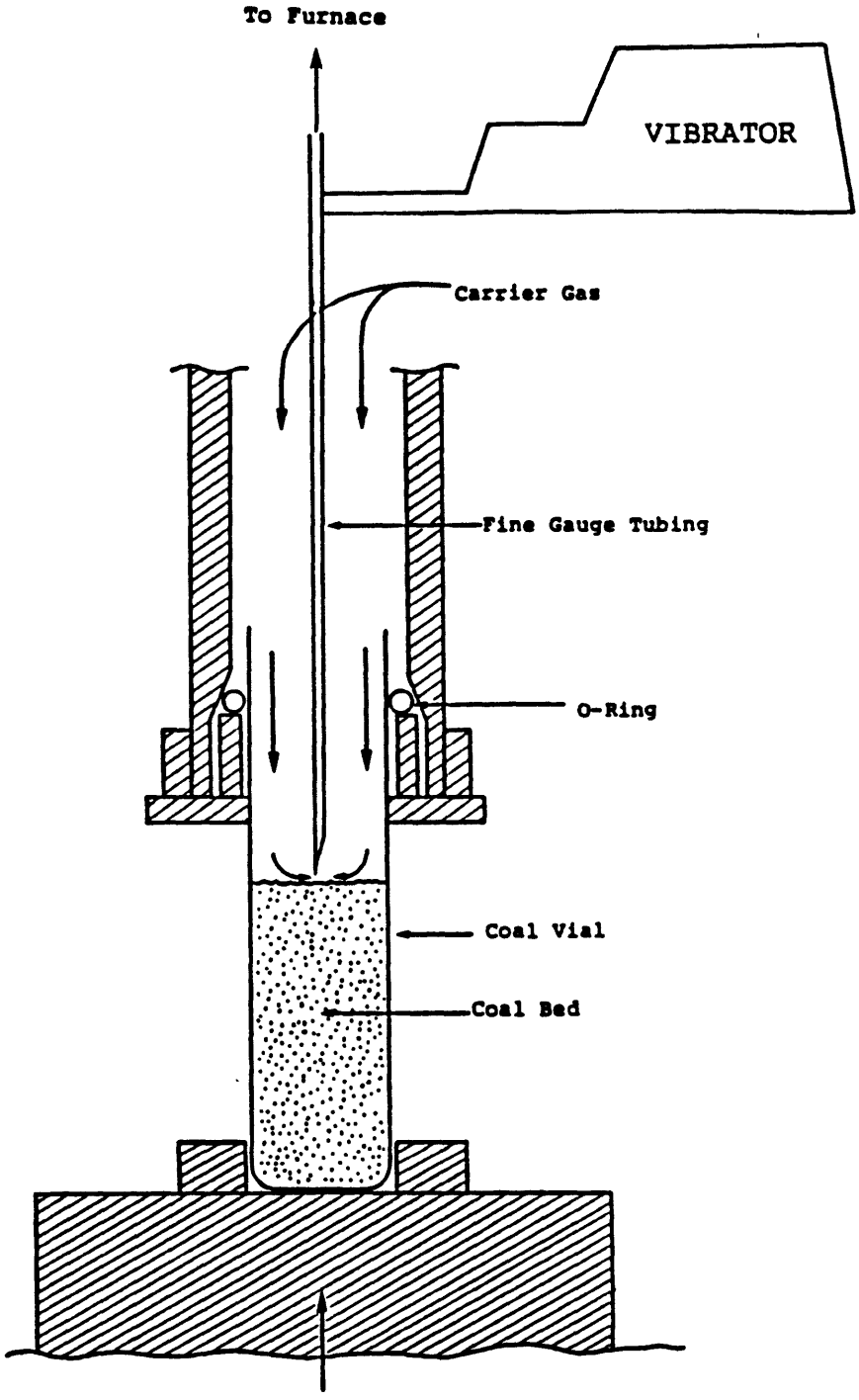

Figure 8. Schematic Diagram of Coal Feeding System

which is inserted through the bottom of the furnace. The probe position is adjustable to enable time-resolved studies. A schematic diagram of the collection probe is presented in Figure 9. The inner core of the probe is fitted with a stainless steel porous tubing through which gas is transpired. The 1.27 cm ID porous tubing is constructed from fused five micron stainless steel spheres. In the top 2.5 cm section of the probe the combustion products are rapidly quenched, at a rate of 1.0×10^{-4} °C/s, by a flow of 3.0×10^{-4} m^3/s of nitrogen. A minimal inward radial gas flow of 6.6×10^{-5} m^3/s of nitrogen which corresponds to a gas velocity of 3.5×10^{-3} m/s is maintained through the subsequent section of porous tubing to counter the thermophoretic velocity of the particles (e.g., 1.8×10^{-4} m/s), thereby preventing particle deposition on the inner wall of the probe.

2.2.4. Two-Color Pyrometer

Figure 6 shows the schematic diagram of the two-color pyrometer[6] used to measure the radiation from the burning particles. A lens located at the bottom of the laminar flow reactor is used to focus the radiation from the burning particles. The particles are viewed against a dark background consisting of a water-cooled collection probe. The signals are measured by individual photomultiplier tubes, after passage through filters with effective wavelengths of 450 and 550 nm and band widths of 5 and 7 nm.

The system was calibrated with a tungsten strip lamp, and provides a temperature resolution of 30 K at 3500 K.

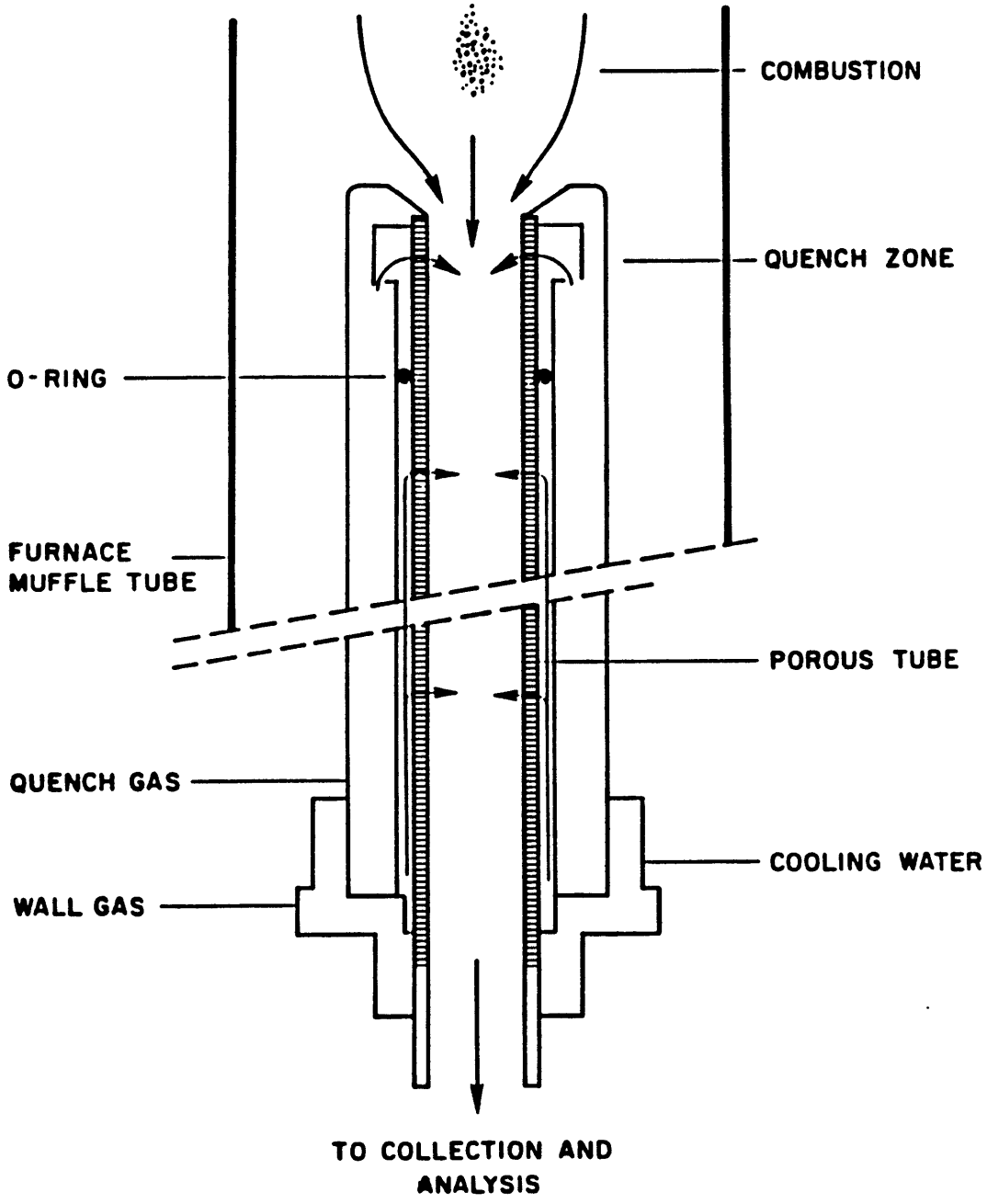

Figure 9. Schematic Diagram of Water-Cooled Collection Probe

CHAPTER 3. EXPERIMENTAL RESULTS

Based on high speed cinematography and from radiation intensity traces, the different stages in the CWF droplet combustion process (Figure 10) can be described as follows:

* Injections of the CWF droplet
* Drying of the CWF droplet
* Agglomeration and swelling during the coal plasticity period
* Localized ignition followed by spread of ignition
* Volatile flame formation
* Rotation induced by volatile evolution
* Extinction of volatile flame and ignition of char
* Fragmentation both during devolatilization and char burnout
* Ash shedding and completion of char burnout

The novel features of the results are the high frequency of rotation and the fragmentation of the particles, which have important ramifications on the space requirements for combustion and the problems of erosion due to ash. The different stages in the CWF droplet combustion process, described above, will be discussed in detail in sections 3.1 to 3.6.

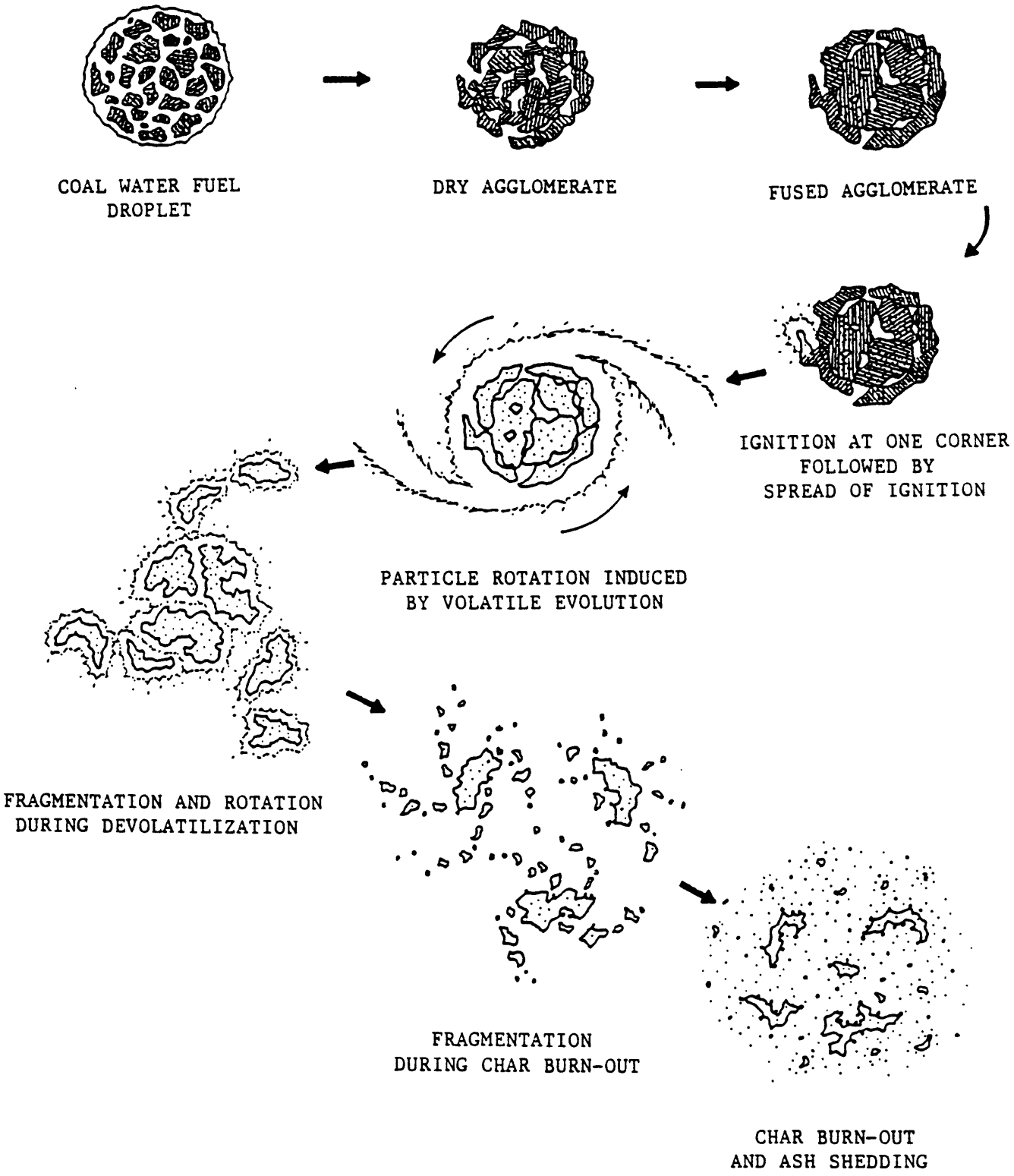

Figure 10. Mechanisms of CWF Droplet Combustion

3.1. Ignition

Upon injection of the CWF droplet into the furnace, the water evaporates. Transmission light photographs show that particles within a droplet adhere, due to surface tension and capillary forces. Once the outer film of water is removed the coal particles on the surface are exposed to the hot environment. The particles become plastic and fuse on the outer perimeter of the agglomerate. Due to the spatially non-uniform heating of the agglomerate, volatile evolution, and hence ignition, occurs locally at one corner of the agglomerate, quickly followed by spread of ignition to the whole surface.

3.2. Volatile Combustion

If the volatile evolution is fast enough to displace oxygen from the particle surface an envelope flame forms around the particle. The visible light emission is radiation from the soot formed by cracking of hydrocarbon species in the fuel-rich region between the particle surface and the flame envelope. During this period, the char agglomerates are shielded from oxygen by the volatile and soot, but are heated by the energy fed back to the surface by the envelope flame. The radiation from the burning particles is predominantly from soot particles in the high temperature zone near the flame front. The char particle surface temperature is relatively low compared to the flame temperature, as evidenced by the dark core at the center of the envelope flame in the high speed photographs.

Measurements of the radiation emitted by particles burning in suspension, dilute enough that only one particle at a time is in the field of view, provide information about the different aspects of the combustion process. Figure 11 shows a typical trace for the combustion of CWF agglomerates. The first major spike corresponds to the devolatilization of coal and the second to char burnout.

The duration of the volatile flame ranged from 5 ms at 100% O_2 to 8 ms at 70% O_2 and 11.9 ms at 50% O_2 for a mean agglomerate size of 83 μm and a gas temperature of 1200 K. There was good correspondence in the volatile combustion times between the in-situ generated particles (5.02 ms at 100% O_2) and re-injected flame agglomerates (5.34 ms), suggesting that the latter could be substituted for further experimentation. At low oxygen concentrations (less than 20% O_2) the volatiles evolved do not burn in a sharp flame envelope; rather, they undergo oxidation in the bulk gas phase resulting in the formation of diffuse soot clouds and trails.

3.3. Particle Rotation

Some fraction of the volatiles is evolved from the agglomerate in the form of jets. The centrifugal force generated from the momentum of the tangentially issuing jets imparts rotation to the particle. High speed cinematography shows that the particles rotate randomly in both clockwise and counter-clockwise fashion, sometimes even changing their spin direction during volatile

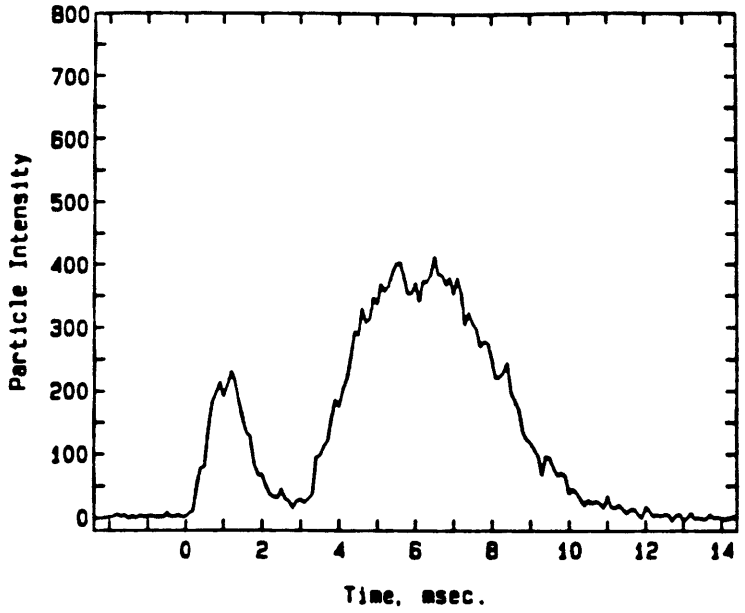

Figure 11. Radiation Emitted by Burning Coal Particle, Showing Devolatilization and Char Burnout

evolution. Particle rotation can also be discerned from the intensity traces of radiation emitted by the devolatilizing/burning particles. Selected particles show periodic oscillations as illustrated in Figure 12. These rotations correspond to non-spherical particles, which therefore exhibit a varying cross-section upon rotation. Frequencies in Figures 12a, 12b, and 12c are approximately 845, 1000, and 1375 cycles/sec, respectively. A rotation frequency of 1000 cps for a 50 μm diameter particle generates centrifugal force at the particle surface of 100 G. This can promote separation of weakly adhering coal particles in the agglomerate, and of fine ash particles and fragments of char from a parent particle. Heat and mass transfer rates to the particle are, however, not significantly affected because of the relatively small rotational slip velocities (0.16 m/sec for a 50 μm diameter particle, 1000 cps) between the particle surface and the gas.

3.4. Ignition of Char

When the rate of volatile evolution decreases, towards the end of the devolatilization step, the flame front recedes and eventually the particle is extinguished. The devolatilized coal (char agglomerate) is heated, predominantly by the ambient gas, till the oxidation reaction becomes fast enough and the particle reignites. This ignition delay or heat-up time between the devolatilization and the oxidation step is a function of the gas temperature and the oxygen mole fraction. It varies from about 7

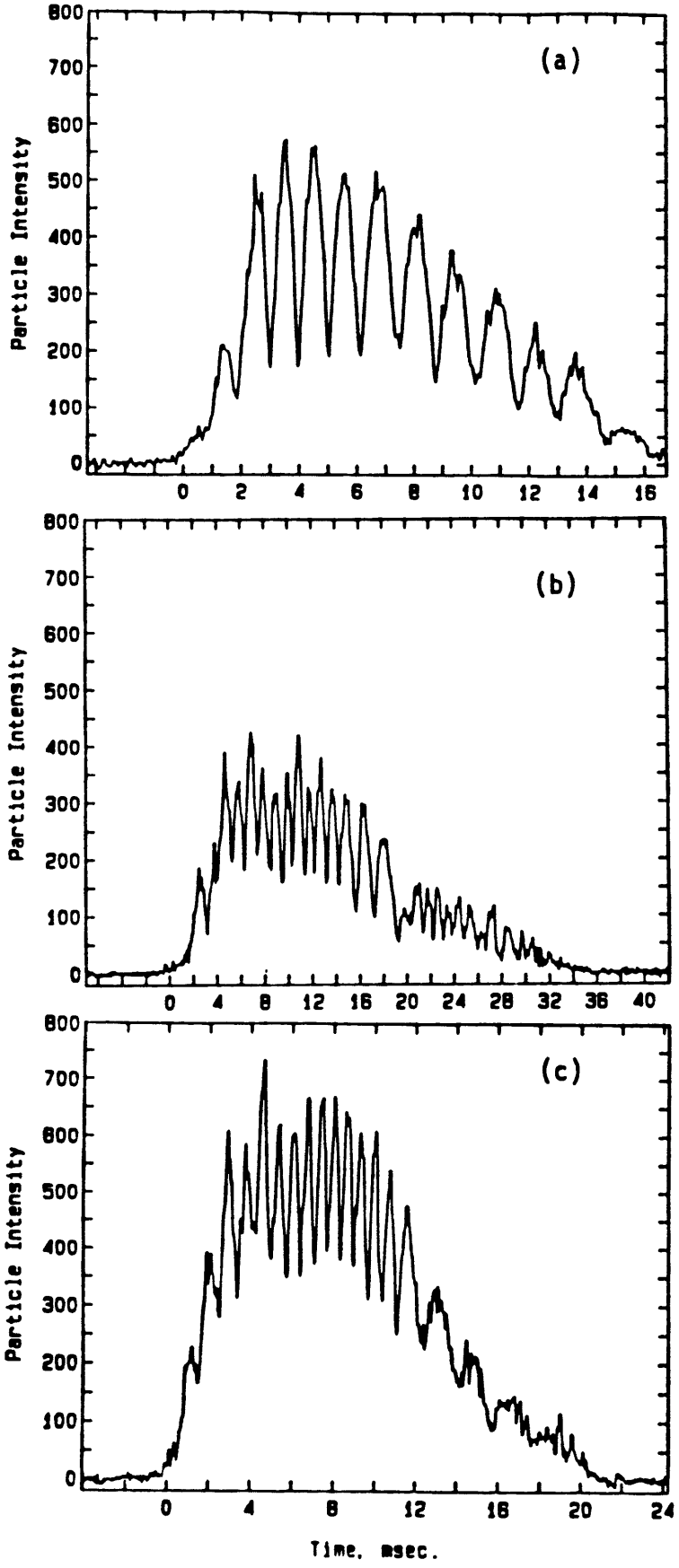

Figure 12. Radiation Emitted by Burning Coal Particles, Showing Periodic Fluctuations Attributable to Particle Rotation

ms at 21% O_2 mole fraction to a fraction of a millisecond at 70% O_2 for a mean agglomerate size of 83 μm at a gas temperature of 1200 K.

3.5. Char Burnout

The estimation of char burnout times, either from high speed cine-films or from photomultiplier signals, is straightforward (e.g., see Figure 11, in which char combustion generates the second major spike). The rate of temperature increase on ignition is very rapid, which implies that the time delay before onset of a detectable optical signal is very short compared to the total combustion time. Similarly, the disappearance of the optical signal due to cooling of the particle essentially coincides with the completion of combustion, ensuring that the overall char burnout time is relatively well defined.

The temperature overshoot for the particle increases with increasing O_2 mole fraction for a given gas temperature, and there is a corresponding increase in burning rate. Consequently, it is seen that a 75-90 μm agglomerate has a burnout time of 36.3 ms at 50% O_2 and 20 ms at 70% O_2 for a gas temperature of 1200 K. Again, char burnout times for in-situ generated and re-injected particles show good agreement, corroborating the similarity between the two cases[7].

3.6. Fragmentation

The other important phenomenon, the extent of which increases with increasing O_2 mole fraction in the gas, is fragmentation.

Fragmentation of the agglomerate is seen to occur during both devolatilization and char burnout. During devolatilization the fragmentation is mainly a bulk phenomenon (as shown in Figure 10), whereas during char burnout both bulk and percolative modes can be important. Some of the radiation traces (Figure 13) show bursts in intensity. These increases in radiant emission can be attributable to the increase in the projected area of the radiating mass which accompanies the fragmentation events. The above inference drawn from the intensity traces is confirmed by the high speed photographic records of the combustion history of the particles.

The particle time-temperature history is seen to be important in determining the extent of fragmentation. From the viscosity-temperature relationship it is seen that, at higher heating rates, the period of plasticity of bituminous coals becomes shorter[8]. It is conceivable that, during pyrolysis, high heating rates could result in agglomerates with lower bond strength; the excess pressure from the combination of trapped water vapor and volatiles generated within could break up such agglomerates into their constituent coal particles. The extent of this bulk fragmentation phenomenon will strongly determine the benefits of grinding the coal to a smaller size.

Fragmentation is also seen during char burnout of the agglomerates. In parallel experiments, coal particles and CWF agglomerates of the same size were burnt under the same combustion conditions. Negligible fragmentation was seen for the coal

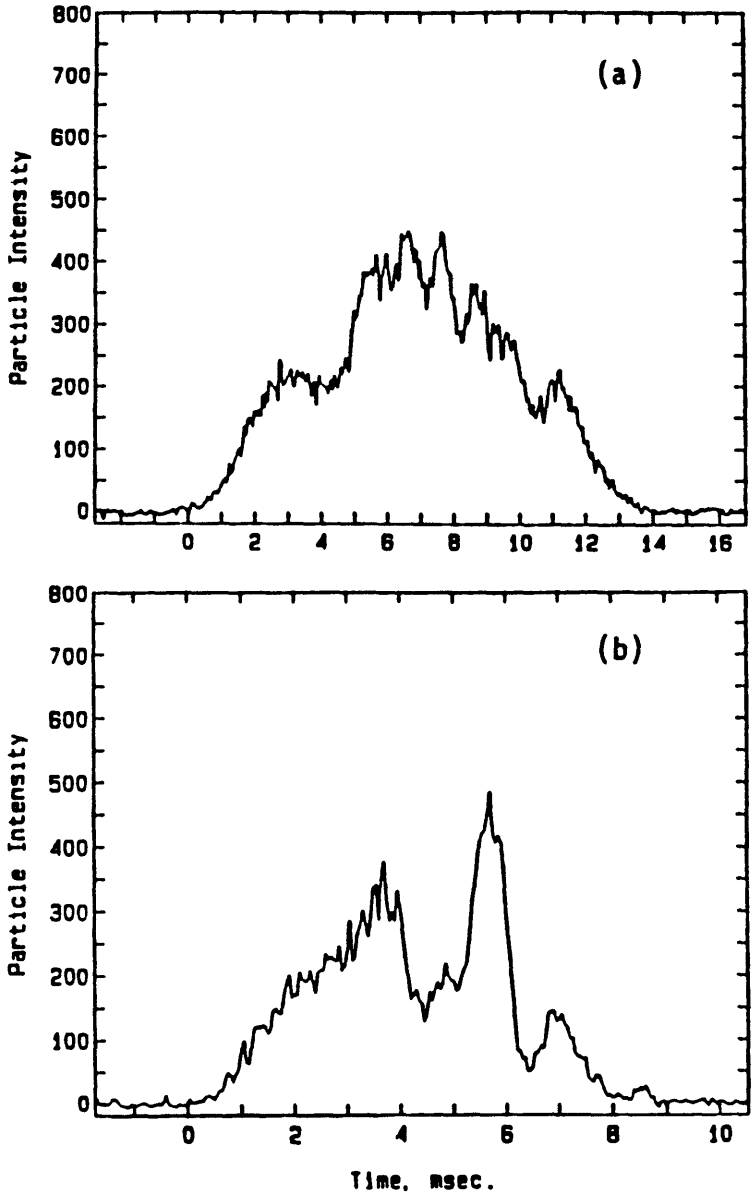

Figure 13. Radiation Emitted by Burning Coal Particles, Showing Fluctuations Attributable to Particle Fragmentation

particles, as opposed to extensive fragmentation, during both pyrolysis and char oxidation, for the CWF agglomerates. Clearly, the fragmentation phenomenon is strongly dependent both on the agglomerate formation process and on the time-temperature history of the particle. Holve et al.[9] using a single particle counter have followed the size of particles generated by combustion of CWF droplets injected into a premixed methane-air flame. They report that no significant particle fragmentation occurs during combustion. It is, therefore, important to determine the conditions under which fragmentation is favored since fragmentation is useful both from the point of view of burnout and in obtaining finer fly-ash size distribution. Increasing the extent of fragmentation will reduce considerably the time required for the burnout of the agglomerates and decrease the size of fly-ash particles because of their origin from smaller parent fragments, thus enhancing the potential benefits of grinding the coal to a finer size[10].

CHAPTER 4. THEORETICAL MODELS

4.1. Model of Particle Rotation

4.1.1. Introduction

During the devolatilization process, some fraction of the volatiles, evolved from the CWF particle in the form of jets, imparts rotation to the CWF particle. The results of high speed cinematography and two-color pyrometry show CWF particle rotation during devolatilization and char burnout.

The centrifugal force, generated from the resultant angular momentum due to the tangential component of the issuing volatiles jets, can promote separation of weakly adhering coal particles from a CWF particle during devolatilization, and of fine ash particles and fragments of char from a parent particle during char burnout. The angular velocity of a CWF particle, which is directly related to the centrifugal force, is correlated with volatile yield and rate of volatile evolution.

4.1.2. Derivation of Angular Velocity of Rotating CWF Particle

Figure 14 shows the schematic diagram of the rotating CWF particle. In this rotation model, the CWF particle is assumed to be spherical, and the exit velocity of volatiles at each devolatilization pore is assumed to be uniform.

The angular momentum of the CWF particle is generated by the tangential component of the issuing volatiles jet, which is expressed by the angles Φ_i and θ_i. The angle Φ_i is defined as

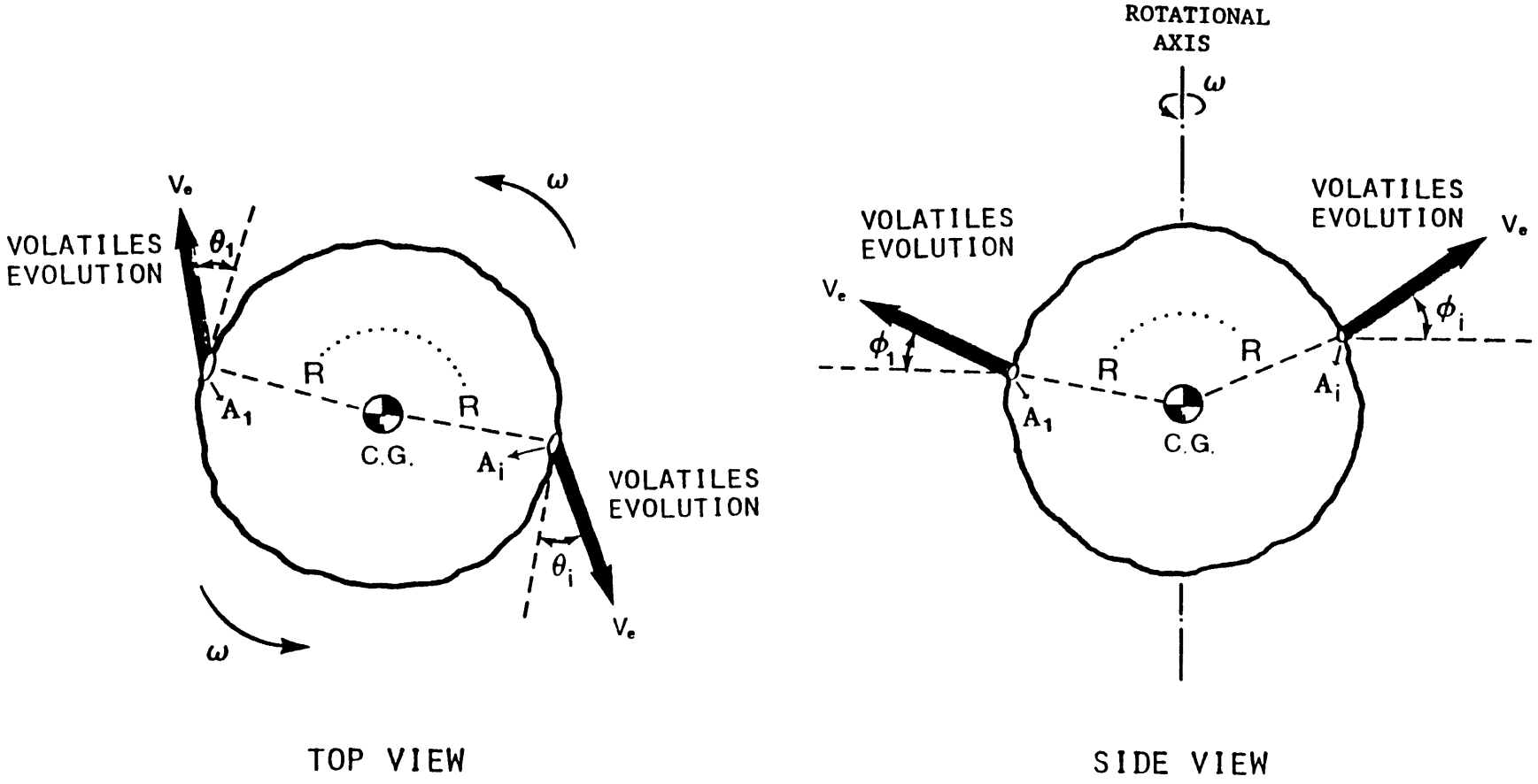

Figure 14. Control Volume of Rotating CWF Particle

the angle between the issuing volatiles jet and the plane which is perpendicular to the rotational axis, and θ_i is the angle between the issuing volatiles jet and the tangential plane at the devolatilization pore exit. The tangential component of the jet velocity of the issuing volatiles is expressed as

$$(v_e)_{tangential} = v_e \cos \theta_i \cos \Phi_i \qquad (1)$$

Here, the exit velocity of volatiles v_e at devolatilization pores is derived as

$$v_e = \frac{M_o\left(\frac{dV}{dt}\right)}{\rho_{vol} \sum_{i=1}^{n} A_i} \qquad (2)$$

where $\sum_{i=1}^{n} A_i$ is the total cross-sectional exit area of devolatilization pores, which can be obtained from the experimental data. The rate of mass loss of volatiles per unit original particle mass is given by dV/dt, while M_o and ρ_{vol} denote the original mass of the CWF particle and the density of the volatiles, respectively.

To obtain the correlation of angular velocity of a particle, the angular momentum equation is applied, as follows:

Angular Momentum Equation

$$\frac{d}{dt}\left(\int_{cv} \vec{r}_{cv} \times \rho_{cv} \vec{v}_{cv} \, d\vec{\forall}\right) + \int_{cs} \vec{r}_{cs} \times \vec{v}_{cs} \rho_{cs} (\vec{v}_{rel} \cdot \vec{n}) \, d\vec{A} = \sum \vec{T} \qquad (3)$$

where $\vec{r}_{cv} = r\vec{i}_r$ $\qquad$ $\vec{r}_{cs} = R\vec{i}_r$

$\vec{v}_{cv} = r\omega\vec{i}_\theta$ $\qquad$ $\vec{v}_{cs} = (R\omega - v_e\cos\theta_i\cos\Phi_i)\,\vec{i}_\theta$

$\vec{r}_{cv} \times \vec{v}_{cv} = r^2\omega\vec{i}_z$ $\qquad$ $\vec{r}_{cs} \times \vec{v}_{cs} = R(R\omega - v_e\cos\theta_i\cos\Phi_i)\vec{i}_z$

$\vec{v}_{rel}$: relative velocity

$\vec{i}_r$: r-directional unit vector

$\vec{i}_\theta$: θ-directional unit vector

$\vec{i}_z$: z-directional unit vector

$\vec{T}$: torque vector acting on particle

t : time

CV : control volume

CS : control surface

The angular momentum equation for the rotational axis of the CWF particle is:

$$\frac{d}{dt}\left(\int_{cv}\rho_A r^2\omega\, d\forall\right) + \int_{cs} R\,(R\omega - v_e\cos\theta_i\cos\Phi_i)\,\rho_{vol}v_e dA = -T_F \qquad (4)$$

Here, T_F denotes the frictional drag of the particle during particle rotation. According to Lamb[11], the frictional drag of the particle during particle rotation for the low Reynolds number flow condition is expressed as

$$T_F = 8 \pi R^3 \mu_{vol} \omega \qquad (5)$$

where R, μ_{vol}, and ω denote radius of the CWF particle, viscosity of volatiles, and angular velocity of the CWF particle, respectively.

The above expression for the frictional drag applies when the rotational Reynolds number Re_r is smaller than five[12]; i.e., when

$$Re_r = \frac{\rho R^2 \omega}{\mu} << 5$$

where ρ and μ denote the density and the viscosity, respectively, of the surrounding gas.

From eq. (4) and (5), the angular momentum equation is expressed as:

$$\frac{d\omega}{dt} + \left[\frac{1}{\rho_A} \frac{d\rho_A}{dt} + \frac{\rho_{vol} v_e \left(\sum_{i=1}^{n} A_i \right)}{\frac{4}{5} \pi R^3 \rho_A} + \frac{10 \mu_{vol}}{\rho_A R^2} \right] \omega$$

$$= \frac{5 \rho_{vol} v_e^2}{4 \pi R^4 \rho_A} \left[\sum_{i=1}^{n} A_i \cos\theta_i \cos\Phi_i \right] \qquad (6)$$

Here, ρ_A denotes the density of the CWF particle at time t. During the devolatilization process, ρ_A can be expressed as:

$$\rho_A = \frac{M_o[1-V]}{\frac{4}{3} \pi R^3} \qquad (7)$$

where M_o is the original CWF particle mass, and V is the mass of volatiles evolved up to time t per unit original CWF particle mass. The swelling of a CWF particle during devolatilization is not considered, and, therefore, the particle radius R is assumed to remain constant. The first derivative of ρ_A is expressed as

$$\frac{d\rho_A}{dt} = \frac{-M_o \left[\frac{dV}{dt}\right]}{\frac{4}{3}\pi R^3} \tag{8}$$

From eq. (2), (6), (7), and (8), the differential equation for the angular velocity of the CWF particle is:

$$\frac{d\omega}{dt} + \left[\frac{\frac{2}{3}M_o\left(\frac{dV}{dt}\right) + \frac{40}{3}\pi R \mu_m}{M_o(1-V)}\right]\omega = \frac{5M_o}{3R\rho_m \sum_{i=1}^{n} A_i}\left[\frac{\sum_{i=1}^{n} A_i \cos\theta_i \cos\phi_i}{\sum_{i=1}^{n} A_i}\right]\frac{\left(\frac{dV}{dt}\right)^2}{(1-V)} \tag{9}$$

The factor $\left[\frac{\Sigma A_i \cos\theta_i \cos\phi_i}{\Sigma A_i}\right]$ is dependent on the geometry and area of the individual devolatilization pores.

The initial condition is

$$\omega(0) = 0 \tag{10}$$

From eq. (9) and (10), the angular velocity of the rotating CWF particle is:

$$\omega(t) = \frac{5 M_o}{3 R \rho_{wd} \sum_{i=1}^{n} A_i}\left[\frac{\sum_{i=1}^{n} A_i \cos\theta_i \cos\phi_i}{\sum_{i=1}^{n} A_i}\right] \exp\left[-\int_0^t \frac{\frac{2}{3} M_o\left(\frac{dV}{dt}\right) + \frac{40}{3}\pi R \mu_{wd}}{M_o (1-V)}\, dt\right]$$

$$\times \int_0^t \left[\frac{\left(\frac{dV}{dt}\right)^2}{(1-V)} \exp\left[\int_0^t \frac{\frac{2}{3} M_o\left(\frac{dV}{dt}\right) + \frac{40}{3}\pi R \mu_{wd}}{M_o (1-V)}\, dt\right]\right] dt \qquad (11)$$

In the above, V and $\frac{dV}{dt}$ are obtained from a devolatilization model.

4.1.3. Angular Velocity of Rotating CWF Particle for an Isothermal Devolatilization Process

To simplify the general correlation (eq. (11)) of the angular velocity of a CWF particle during devolatilization, the following assumptions are added:

(1) The CWF particle temperature, and therefore the devolatilization rate constant, are assumed to remain constant during devolatilization (i.e. isothermal devolatilization);

(2) The devolatilization process is assumed to be described by the following global single reaction model:

$$\frac{dV}{dt} = k\ (V^* - V)$$

where, k = devolatilization rate constant

and where V and $\frac{dV}{dt}$ have been defined in Section 4.1.2.

Based upon the above additional assumptions, the volatiles mass loss per unit original particle mass is derived as

$$V = V^* \{1 - \exp(-kt)\},$$

and then

$$\frac{dV}{dt} = kV^* \exp(-kt) \tag{12}$$

From eq. (2) and (12), exit velocity of volatiles evolved at time t is derived as

$$v_e = \frac{M_o \left(\frac{dV}{dt}\right)}{\rho_{vol} \sum_{i=1}^{n} A_i} = \frac{M_o\, k\, V^* \exp(-kt)}{\rho_{vol} \sum_{i=1}^{n} A_i} \tag{13}$$

From eq. (4), (5), and (13), the angular momentum equation for the rotational axis of the CWF particle is

$$\frac{d}{dt}\left(\frac{4}{5}\pi R^5 \rho_A \omega\right) + \sum_{i=1}^{n} R\left(R\omega - v_e \cos\theta_i \cos\Phi_i\right) \rho_{vol} v_e A_i = -8\pi R^3 \mu_{vol} \omega \tag{14}$$

Here, the density ρ_A of the CWF particle at time t is

$$\rho_A = \frac{M_o \left[1 - V^* \{1 - \exp(-kt)\}\right]}{\frac{4}{3}\pi R^3} \tag{15}$$

From eq. (13), (14), and (15), the differential equation for the angular velocity of the CWF particle is

$$\frac{d\omega}{dt} + \left[\frac{c_1 \exp(-kt) + c_2}{c_3 \exp(-kt) + c_4}\right]\omega = \frac{c_5 \exp(-2kt)}{c_3 \exp(-kt) + c_4} \qquad (16)$$

where $c_1 = \frac{2}{3} M_o V^* k$

$c_2 = \frac{40}{3} \pi R \mu_{vol}$

$c_3 = M_o V^*$

$c_4 = M_o (1 - V^*)$

$$c_5 = \frac{5 M_o^2 V^{*2} k^2}{3 R \rho_{vol} \sum_{i=1}^{n} A_i} \left[\frac{\sum_{i=1}^{n} A_i \cos\theta_i \cos\Phi_i}{\sum_{i=1}^{n} A_i}\right]$$

From eq. (10) and (16), the angular velocity of a CWF particle for an isothermal devolatilization process and a devolatilization model of a global single reaction is

$$\omega(t) = \frac{\frac{5 M_o^2 V^{*2} k^2}{3 R \rho_{vol} \sum_{i=1}^{n} A_i} \left[\frac{\sum_{i=1}^{n} A_i \cos\theta_i \cos\phi_i}{\sum_{i=1}^{n} A_i}\right]}{\left[M_o\{V^* \exp[-kt] - V^* + 1\}\right]^{\left[\frac{40 \pi R \mu_{vol}}{3 M_o \{1-V^*\} k} - \frac{2}{3}\right]} \exp\left[\frac{40 \pi R \mu_{vol} t}{3 M_o \{1-V^*\}}\right]} \qquad (17)$$

$$\times \int_0^t \left[\left[M_o\{V^* \exp[-kt] - V^* + 1\}\right]^{\left[\frac{40 \pi R \mu_{vol}}{3 M_o \{1-V^*\} k} - \frac{5}{3}\right]} \exp\left[\frac{40 \pi R \mu_{vol} t}{3 M_o \{1-V^*\}} - 2kt\right]\right] dt$$

4.1.4. Centrifugal Force induced by Particle Rotation

The centrifugal force acting on a coal particle of mass m_c on the outer edge of an agglomerate of radius R (Figure 15) can be obtained by substituting the angular velocity $\omega(t)$, obtained from eq. (11) or (17), into:

$$F_{centrif} = m_c R[\omega(t)]^2 \qquad (18)$$

4.2. Model of Particle Agglomeration

4.2.1. Introduction

Upon injection of the CWF droplet into the furnace, the interstitial water of the CWF droplet begins to evaporate. As this occurs, the individual coal particles become exposed to the hot environment and are heated up rapidly. On heating to about 400°C or above, bituminous coal particles become plastic and fuse. The extent of agglomeration depends on the duration of the plastic period which is strongly affected by both the time-temperature history of the coal particles and the coal type.

When the duration of the plastic period is long enough for particles to fuse and coalesce, strongly-fused CWF agglomerate will be formed. Due to strong adhesive forces between adjacent coal particles, the CWF agglomerates will be difficult to fragment, which results in poor combustion.

In contrast, when the duration of the plastic period is too

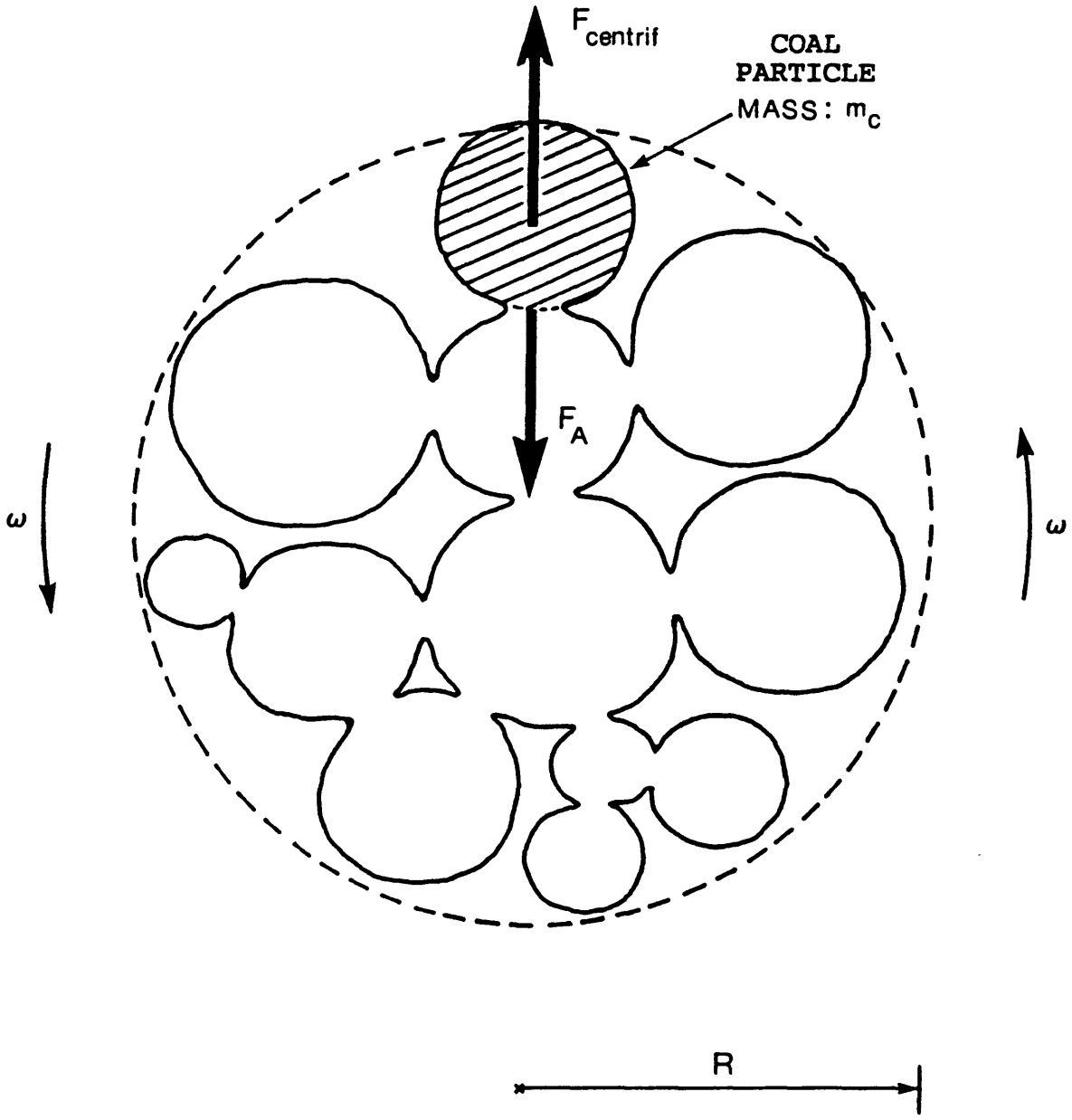

Figure 15. Force Balance during CWF Agglomerate Rotation

short for particles to fuse and completely coalesce, loosely-fused CWF agglomerate will be formed, the adhesive forces between contiguous coal particles will be weak, and the agglomerates will break up, resulting in better combustion. Consequently, the plasticity-time history of the coal particles is found to be important for the study of CWF particle agglomeration.

4.2.2. Plasticity of Bituminous Coal

Upon heating of bituminous coal to about 400°C or above, the transient occurrence of plastic behavior of coal particles can be observed. Earlier "bitumen" theory explains plastic development as a result of a fusible component (bitumen) which melts to provide a viscous slurry. The later "metaplast" theory is more commonly accepted. (Fitzgerald[13], Chermin and Van Krevelen[14]). The liquid metaplast is generated and depleted by the following pyrolytic reactions:

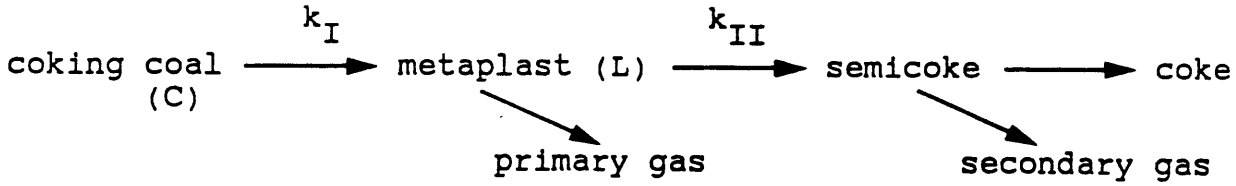

These reactions, which in a simplified form describe coke formation, are the basis for the following mathematical model:

$$\frac{dC}{dt} = - k_I C$$

$$\frac{dL}{dt} = k_I C - k_{II} L$$

The assumption of this mathematical model is that the reactions are first-order. Fong et al.[15] elaborate on this model by taking account of the liquid formed by physical melting. Initially, above a critical temperature, some fraction of liquid is formed by physical melting. With further temperature increase, pyrolytic bond breaking generates additional liquid. Simultaneously, the liquid forms a volatile product which escapes from the coal and leaves a solid coke residue. The reaction scheme and corresponding rate expressions during the plasticity of a bituminous coal particle are[8]:

$$\text{coal } (\tilde{C}) \xrightarrow[\text{physical melting } r_m]{k_I} \underset{\text{metaplast}}{\text{liquid}} \ (\tilde{L}) \xrightarrow{k_{II}} \underset{\text{volatiles } (\tilde{V})}{\text{coke } (\tilde{E}) \ \&}$$

$$\frac{d\tilde{C}}{dt} = - k_I \tilde{C} - r_m \tag{19}$$

$$\frac{d\tilde{L}}{dt} = k_I \tilde{C} + r_m - k_{II} \tilde{L} \tag{20}$$

where $\tilde{C}$ and $\tilde{L}$ are the mass fractions of unreacted coal and liquid metaplast, respectively, and r_m is the rate of physical melting, and k_I and k_{II} are rate constants.

The initial conditions of eq. (19) and (20) are

$$\tilde{C}\ (0) = \tilde{C}_i \tag{21}$$

$$\text{and} \quad \tilde{L}\ (0) = 0 \tag{22}$$

where $\tilde{C}_i \equiv$ initial mass fraction of unreacted coal.

From eq. (19) and (21), the mass fraction of unreacted coal is expressed as a function of the reaction rate constant, k_I, and the physical melting rate, r_m, as follows:

$$\tilde{C} = \exp\left[-\int_o^t k_I\, dt\right]\left[\int_o^t (-r_m)\exp\left[\int_o^t k_I dt\right] dt + \tilde{C}_i\right] \qquad (23)$$

From eq. (20), (22), and (23), the mass fraction of liquid metaplast is derived as:

$$\tilde{L} = \exp\left[-\int_o^t k_{II}dt\right]\left[\int_o^t \exp\left[\int_o^t k_{II}dt\right]\left(r_m + \tilde{C}_i k_I \exp\left[-\int_o^t k_I dt\right]\right.\right.$$

$$\left.\left. + k_I \exp\left[-\int_o^t k_I dt\right]\int_o^t (-r_m)\exp\left[\int_o^t k_I dt\right]dt\right)dt\right] \qquad (24)$$

The rate of physical melting, r_m, is given[15] by the heating rate of a coal particle multiplied by a Gaussian distribution of melting points centered at a mean melting temperature of 623 K with a standard deviation of 30 K.

$$r_m = \left[\frac{L_s}{\sqrt{2\pi}\,\sigma_T}\exp\left\{-\frac{(T_p - T_m)^2}{2\sigma_T^2}\right\}\right]\left(\frac{dT_p}{dt}\right) \qquad (25)$$

where $T_p \equiv$ coal particle temperature

$T_m \equiv$ mean melting temperature of coal particle (= 623 K)

$\left(\frac{dT_p}{dt}\right) \equiv$ heating rate of coal particle

σ_T ≡ standard deviation of melting temperature (= 30 K)

L_s ≡ total amount of solid metaplast initially existing in coal

The rate constants of k_I and k_{II} are obtained from experimental data for a Pittsburgh seam bituminous coal (Fong et al.[15]).

$$k_I = 6.6 \times 10^7 \exp(-14{,}500/T_p) \left[\frac{1}{sec}\right]$$

$$k_{II} = 1.9 \times 10^{10} \exp(-21{,}200/T_p) \left[\frac{1}{sec}\right] \quad (26)$$

In the present study, it is assumed that swelling due to expansion of volatile bubbles in the liquid metaplast is not significant, and therefore, the radius of a coal particle remains constant (i.e. no swelling). It is also assumed that volatile bubbles formed in the liquid metaplast escape instantly and leave micro-porous coke-residue in the liquid metaplast, and that a coal particle during the coalescence process consists of unsoftened coal, liquid metaplast, mineral matter, and coke-residue which has only micropores (not macropores). Based on the above assumptions, the volume fraction of each component will be derived as follows:
The volume fraction of unreacted coal, C, is

$$C = \frac{\rho_o}{\rho_c} \tilde{C} \quad (27)$$

where $\tilde{C}$ denotes the mass fraction of unreacted coal, given by eq. (23), ρ_c denotes the density of unreacted coal, and ρ_o is the initial apparent density of the coal particle, expressed as follows:

$$\rho_o = \frac{\rho_c \rho_a}{\rho_a - \tilde{f}_a (\rho_a - \rho_c)} \tag{28}$$

where ρ_a is the density of mineral matter, and $\tilde{f}_a$ is the mass fraction of mineral matter, given by $\tilde{f}_a = 1 - \tilde{C}_i$.

From eq. (23), (27), and (28), the volume fraction of unreacted coal, C, is expressed as

$$C = \frac{\rho_a}{\rho_a - \tilde{f}_a(\rho_a - \rho_c)} \exp[-\int_o^t k_I dt][\int_o^t (-r_m) \exp[\int_o^t k_I dt]dt + \tilde{C}_i] \tag{29}$$

The volume fraction of liquid metaplast, L, is

$$L = \frac{\rho_o}{\rho_L} \tilde{L} \tag{30}$$

where $\tilde{L}$ denotes the mass fraction of liquid metaplast, given by eq. (24), ρ_L is the density of liquid metaplast, and ρ_o is the initial apparent density of the coal particle, given by eq. (28). From eq. (24), (28), and (30), the volume fraction of liquid metaplast, L, is expressed as

$$L = \frac{\rho_a \rho_c}{\rho_L[\rho_a - \tilde{f}_a(\rho_a - \rho_c)]} \exp[-\int_o^t k_{II} dt][\int_o^t \exp[\int_o^t k_{II} dt]\{r_m + \tilde{C}_i k_I \exp[-\int_o^t k_I dt] + k_I \exp[-\int_o^t k_I dt] \int_o^t (-r_m) \exp[\int_o^t k_I dt]dt\}dt] \tag{31}$$

The volume fraction of mineral matter f_a, is

$$f_a = \frac{\rho_o}{\rho_a} \tilde{f}_a \tag{32}$$

which may be rewritten, using eq. (28), in the form

$$f_a = \frac{\rho_c}{\rho_a - \tilde{f}_a(\rho_a - \rho_c)} \tilde{f}_a \qquad (33)$$

Using the above values for C, L, and f_a, and the previously stated assumption of negligible swelling, the volume fraction of coke E is derived as:

$$E = 1 - C - L - f_a \qquad (34)$$

4.2.3. Contact Area during Particle Agglomeration

During the particle agglomeration, coal particles in the CWF particle fuse and coalesce, and the contact area between adjacent coal particles increases until the liquid metaplast in the coal is depleted completely.

Theoretical calculations of the sintering of a Newtonian viscous fluid, using the approximate flow field of simple uniaxial contraction, have been made by Frenkel[16]. He derived a neck growth rate law for the sintering of two spheres. This law has been verified by other authors[17,18,19] to determine the accuracy of time dependency, and expressed as

$$A = \frac{3}{2} \frac{r\gamma}{\mu} t \qquad (35)$$

where A ≡ contact area at time t

r ≡ radius of coalescent sphere

γ ≡ surface tension of coalescent sphere

μ ≡ apparent viscosity of coalescent sphere

The growth rate, $\frac{dA}{dt}$, of this contact area during the coalescence process for coal particles is expressed as

$$\frac{dA}{dt} = \frac{3}{2} \frac{r\gamma}{\mu} \tag{36}$$

Using a concentrated suspension model of Frankel and Acrivos[20], μ is assumed to depend on μ^*, the viscosity of the solids free liquid, and on (1-L), the volume fraction of solids in the liquid, where L is the volume fraction of liquid metaplast discussed in Section 4.2.2. Their relationship for the apparent viscosity is

$$\mu = \frac{\frac{9}{8} \mu^*}{\{1-L\}^{-\frac{1}{3}} - 1} \tag{37}$$

They found this expression to match well with experimental data over a wide range of volume fraction of solids (i.e. $0.4 < (1-L) < 1.0$).

This implies that $0<L<0.6$, which is compatible with the calculated values of L in the present modeling effort (see Section 5.2). In the present study the value of μ^* is estimated from Nazem's[21] work on carbonaceous mesophase pitch (average value taken). The surface tension of the liquid metaplast decreases with increasing temperature, but the experimental data on coal liquids of Hwang et al.[22] show that the magnitude of this decrease is small compared to the corresponding decrease in viscosity.

Therefore, the surface tension of the liquid metaplast is assumed to be constant in the present study,

$$\gamma = \gamma_c \tag{38}$$

From eq. (36), (37), and (38), the growth rate of the contact area between neighboring coal particles during coalescence is derived as

$$\frac{dA}{dt} = \frac{4}{3} \frac{r_c \gamma_c}{\mu^*} [(1-L)^{-1/3} - 1] \tag{39}$$

where r_c is the coal particle radius.

The initial condition for the contact area A is

$$A(0) = 0 \tag{40}$$

and therefore the contact area A between coal particles during coalescence may be written

$$A = \frac{4}{3} \frac{r_c \gamma_c}{\mu^*} \int_0^t [(1-L)^{-1/3} - 1]dt \tag{41}$$

4.2.4. Adhesive Force during Particle Agglomeration

The adhesive force between two coalescent coal particles during the particle agglomeration is expressed as the sum of the surface tension force due to the liquid metaplast and the adhesive force due to coke interconnection.

4.2.4.1. Surface Tension Force

Figure 16 shows two coalescent coal particles in the CWF agglomerate. The surface tension force due to liquid metaplast in the neck region is proportional to the effective circumference ℓ_{eff} of the neck region, expressed as

$$\ell_{eff} = 2 \pi r^* L \tag{42}$$

where r^* ≡ radius of neck region, given by

$$r^* = \left(\frac{A}{\pi}\right)^{1/2} \tag{43}$$

The surface tension force, F_γ, is

$$F_\gamma = \gamma_C \cos \theta \ \ell_{eff} \tag{44}$$

where θ is the contact angle, taken to be 90° as indicated in Figure 16. Hence, the surface tension force due to the liquid metaplast is derived as

$$F_\gamma = 2 \sqrt{\pi A} \ L \ \gamma_C \tag{45}$$

4.2.4.2. Adhesive Force due to Coke Interconnection

Figure 17 shows the agglomeration process of two coalescent coal particles in the CWF agglomerate, with the period of plasticity being divided into three stages. The classification of each of

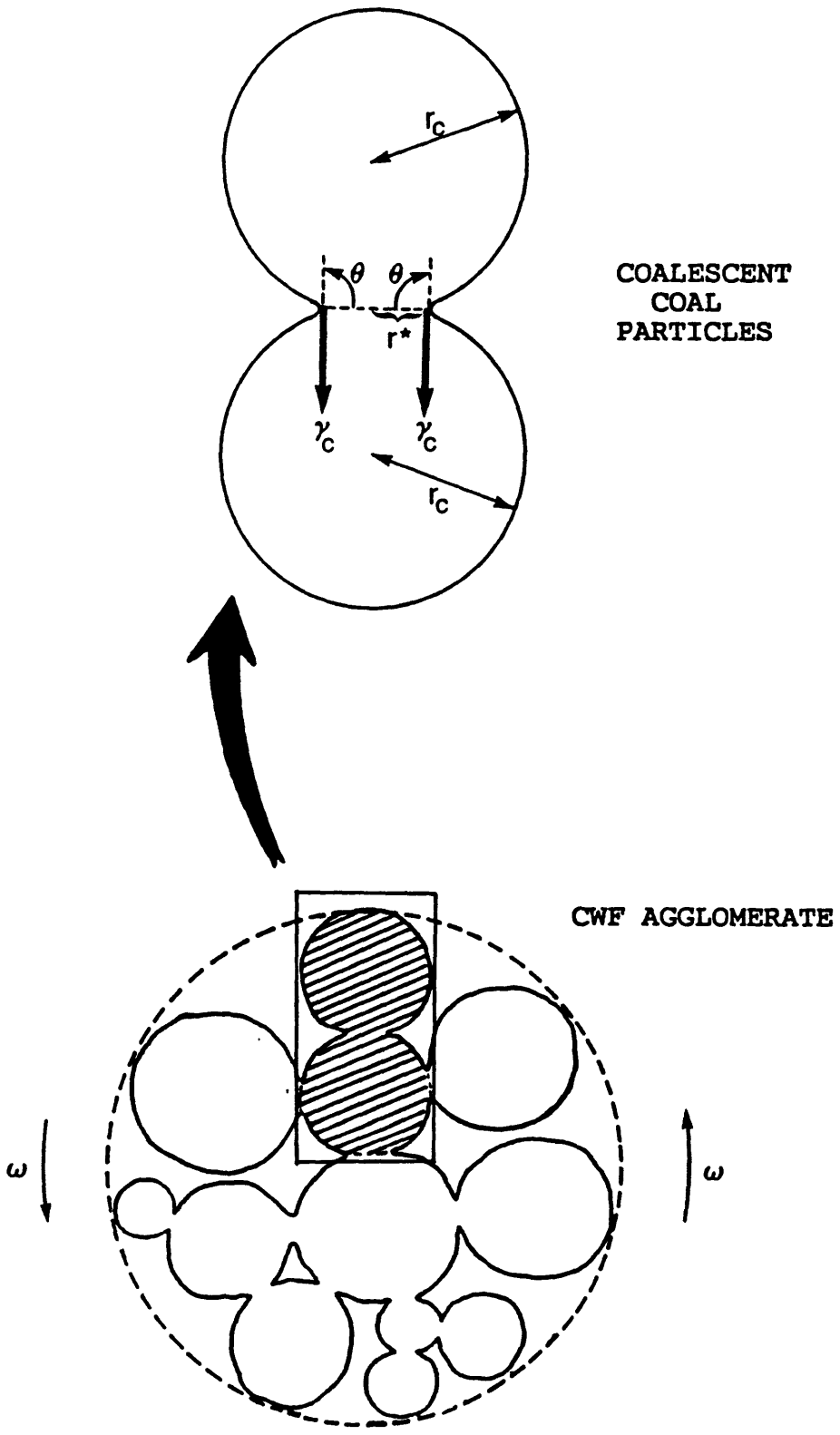

Figure 16. Surface Tension Force at Neck Region of Two Coalescent Coal Particles in CWF Agglomerate

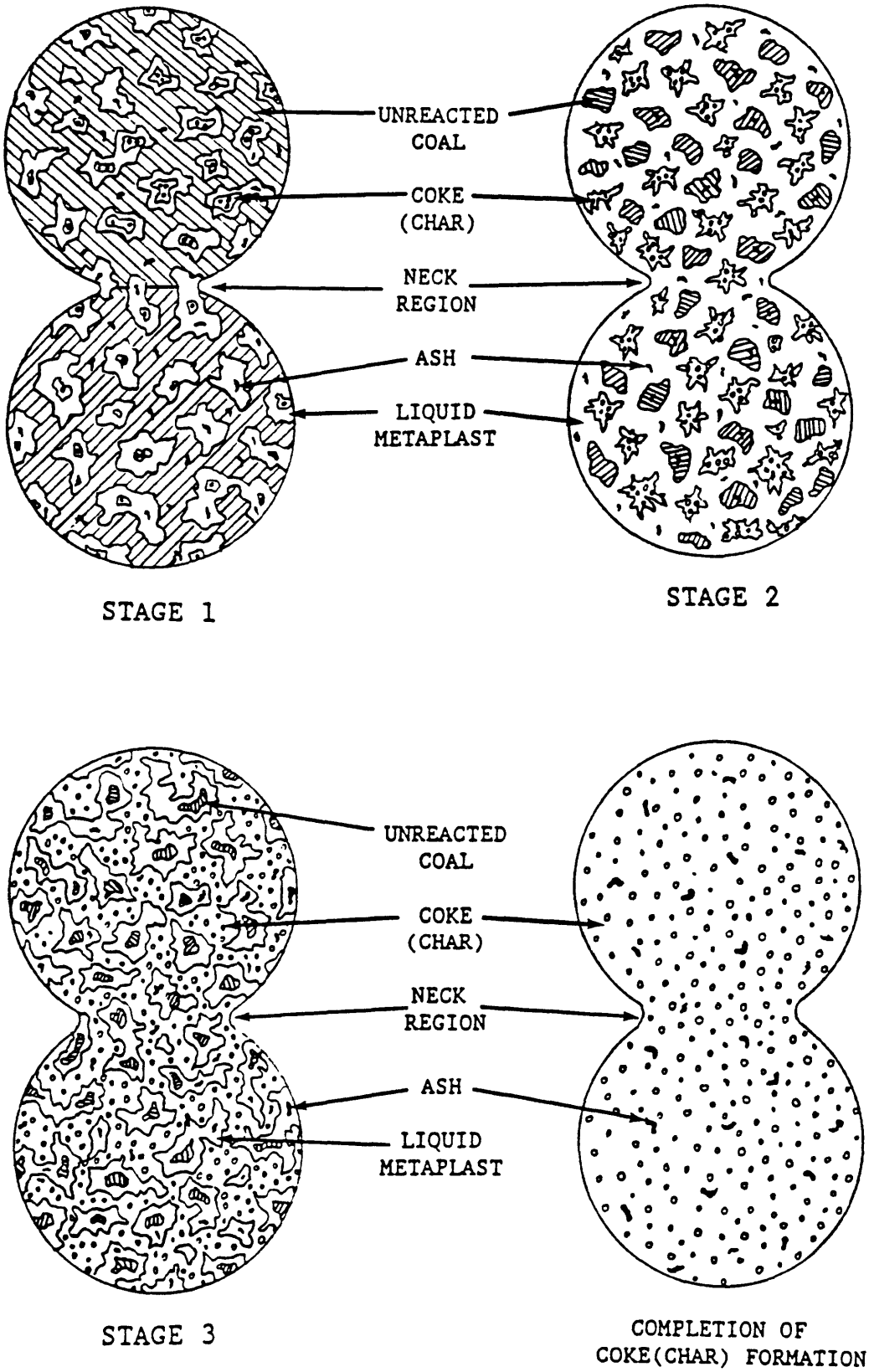

Figure 17. Agglomeration Process of Coal Particles in CWF Agglomerate

these stages depends upon the solids in the suspension of liquid metaplast; these solids are coke & ash, coke & ash & unreacted coal, and unreacted coal & ash, in stages 1, 2, and 3, respectively.

According to Taylor[23] and Friel et al.[24], a characteristic "mosaic" structure of coke is found to develop during the carbonization of vitrinite. The spherical bodies, each of which has a single crystallographic orientation, become enlarged until they begin to interfere with one another's growth as the mosaic-type structure starts to form. Completion of the mosaic formation coincides with completion of the resolidification of the coal. Taylor[23] also found that when the proportion of the coke-residue (char) has been increased to about one half, the spherical bodies begin to interfere with one another's growth. Hence, in the present study, the threshold volume fraction of coke-residue, E_{th}, which is a borderline between stage 2 and stage 3, is defined as 50% of $(1-f_a)$. (i.e. $E_{th} = \frac{1-f_a}{2}$). Therefore, in stage 1 and stage 2, when the volume fraction of coke-residue E is smaller than the threshold volume fraction of coke-residue E_{th}, each mosaic-type coke-residue grows separately, and there is no adhesive force due to coke interconnection. However, in stage 3, when E is larger than E_{th}, the coke-residue starts interlocking and the adhesive force due to interconnection begins to be affected. The coke-residue (char) which is formed after the initiation of the coke interlock strengthens the connections between individual coke crystalline structures. Hence, the adhesive force due to coke interconnection in stage 3, F_{E_3}, is assumed to be proportional to

the fraction of coke-residue (char) which is formed after the initiation of coke interconnection, $E-E_{th}$. Thus this adhesive force is written

$$F_{E_3} = \sigma_E A \left[\frac{E-E_{th}}{1-f_a-E_{th}}\right] \tag{46}$$

in stage 3, where σ_E denotes the bond stress of the coke-residue (char), and the normalizing factor leads to $F_{E_3} \rightarrow \sigma_E A$ when $E \rightarrow E_{max} \equiv 1-f_a$, from Eq. (34). It is also assumed that, in stages 1 and 2:

$$F_{E_1} = F_{E_2} = 0 \tag{47}$$

4.2.4.3. Adhesive Forces during Particle Agglomeration

During the particle agglomeration, the adhesive force F_A between two coalescent coal particles in the CWF agglomerate is expressed as the sum of the surface tension and adhesive forces discussed above. Thus, using eq. (45), (46), and (47), the adhesive force is written

$$F_A = F_\gamma + F_E \tag{48}$$

CHAPTER 5. MODEL PREDICTIONS AND DISCUSSION

5.1. Introduction

When a CWF droplet is injected into the hot combustion zone of the laminar flow reactor (LFR), the droplet is heated up by thermal radiation from the reactor wall and by heat conduction from the ambient surrounding gas (or flame).

Figure 18 shows the typical time-temperature history of a CWF droplet (particle) during CWF combustion. This history can be divided into four stages; evaporation, particle heat-up, devolatilization, and char burnout. It is possible to calculate the temperature and the heating rate of a CWF particle during combustion from the energy balance for the particle.

However, in the application of models derived in Sections 4.1 and 4.2 we have chosen a different approach. In Section 5.2, based on the model of Section 4.1, we use the isothermal devolatilization concept. Then in Section 5.3, using the model of Section 4.2, we impose a constant heating rate on the CWF droplet/particle. Heating rates selected in Section 5.3 are representative of those experienced in CWF combustion, and of those attainable in Laminar Flow Reactors (LFR). A major experimental advantage of the use of an LFR comes from the ability to study individual droplets under a range of heating rates and ambient oxygen concentrations, thus permitting the researcher to study the effects of combustion process modifications on ignition and burnout characteristics of different coal-water fuels.

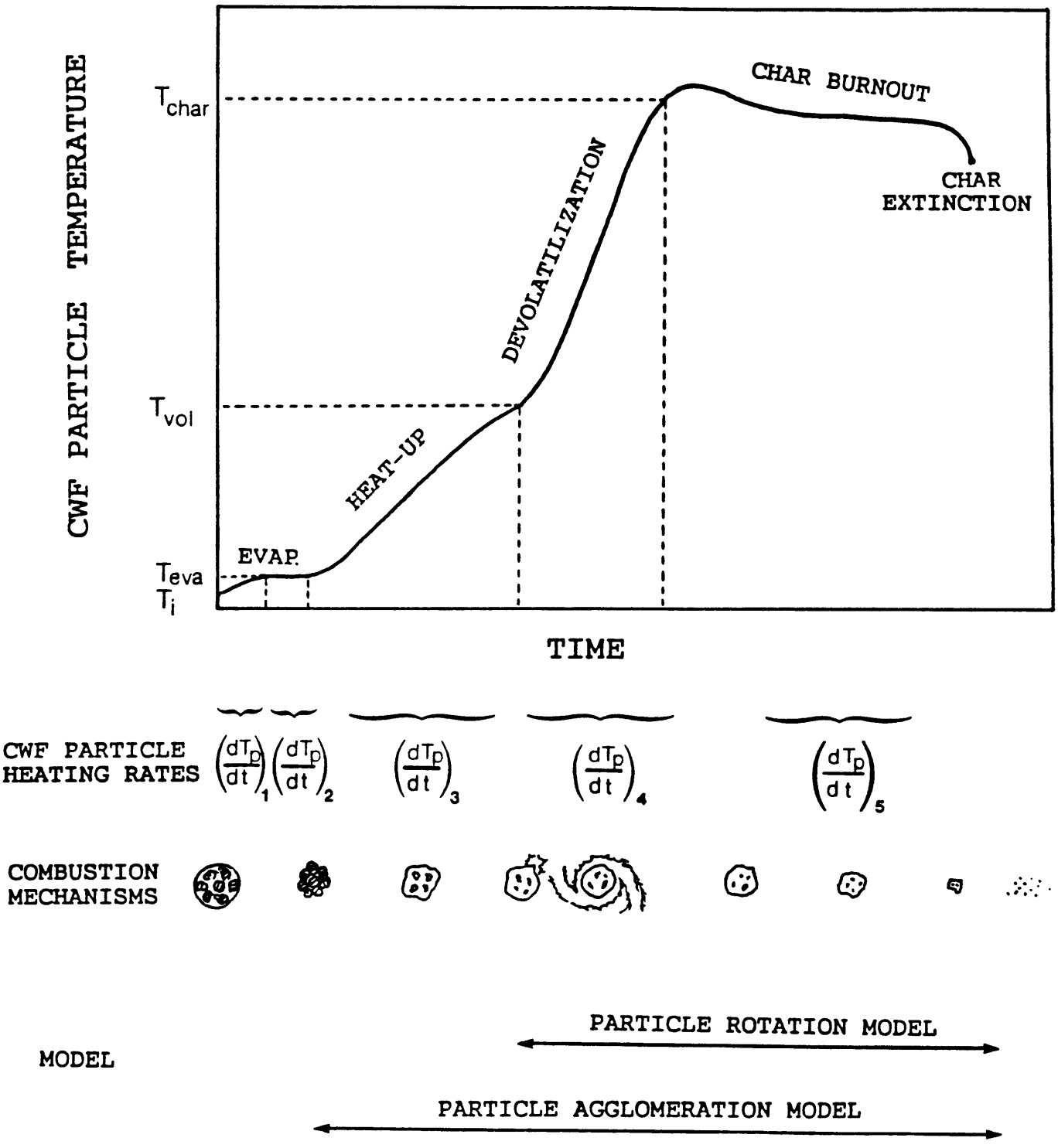

Figure 18. Typical Time-temperature History of CWF Particle during CWF Droplet Combustion

5.2. Particle Rotation

The results of high speed cinematography and two-color pyrometer show that the frequency of particle rotation and the fraction of rotating particles per total burning particles vary with oxygen partial pressure and gas temperature in the laminar flow reactor (LFR).

During the experiments, the oxygen partial pressure ranged from 20% to 100%, and the furnace temperature ranged from 1100 K to 1750 K. As the oxygen partial pressure or the furnace temperature increased, the frequency of particle rotation and the fraction of rotating particles per total number of burning particles increased, and consequently, the extent of fragmentation during devolatilization and char burnout increased. Based upon the above experimental results, it is concluded that the frequency of particle rotation, the fraction of rotating particles per total burning particles, and the extent and frequency of fragmentation are strong functions of particle heating rate and are directly influenced by oxygen partial pressure and gas temperature in the furnace.

The angular velocity of rotating CWF particle during devolatilization and char burnout can be predicted by the model of particle rotation, described by the equations (11) to (17). Figure 19 shows the prediction of the angular velocity of CWF particle for an isothermal devolatilization process as functions of time and particle diameter. The devolatilization rate constant k is assumed to be the same for all different particle sizes in

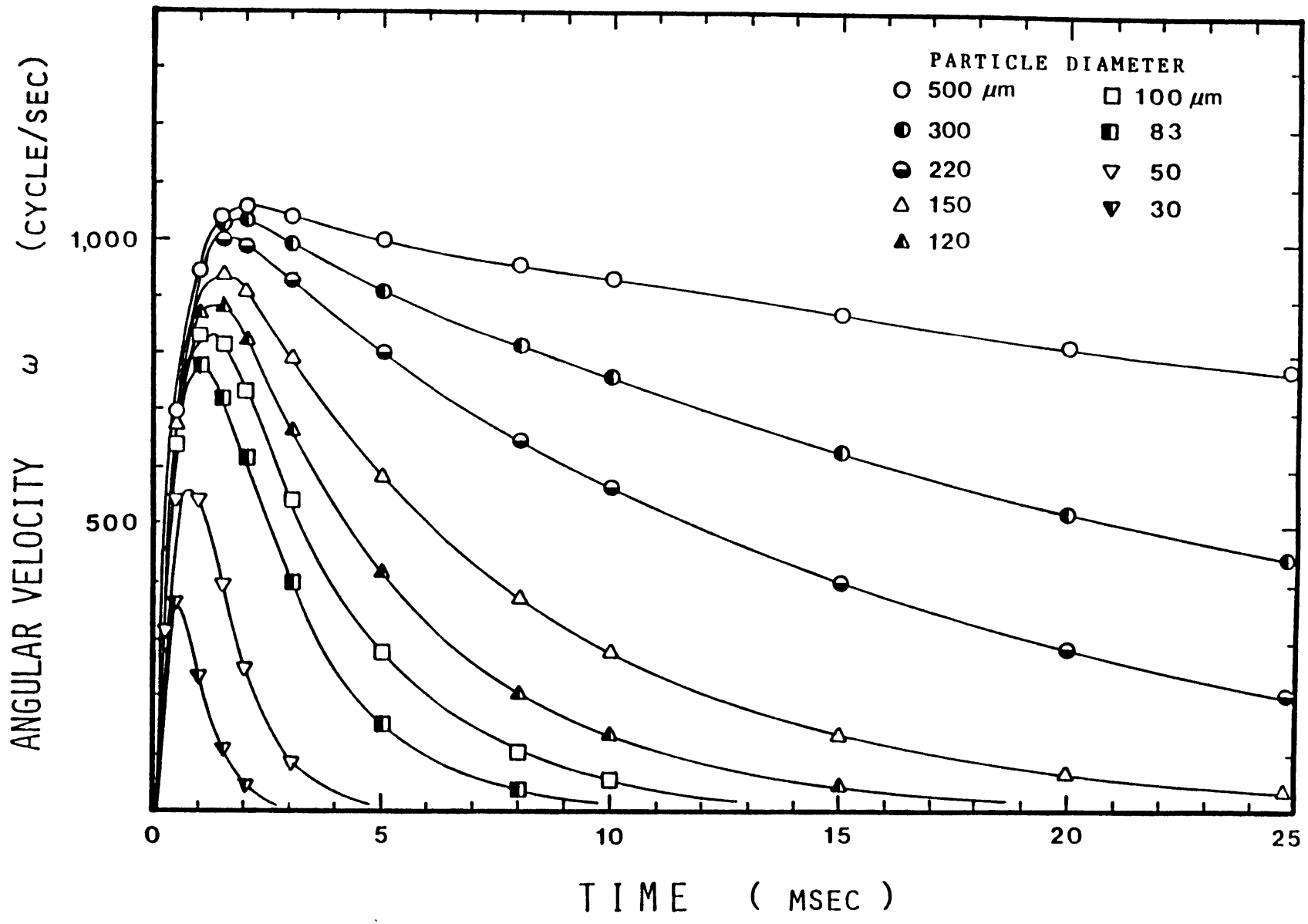

Figure 19. Predictions of Angular Velocity with CWF Particle Size

Figure 19. Figure 20 shows the comparison between the prediction and the experimental data for the oxygen partial pressure of 100%, the furnace temperature of 1200 K, and the particle diameter of 220 μm. It shows a good agreement between the prediction and the experimental data.

5.3. Adhesive Forces during Particle Agglomeration

The adhesive forces during particle agglomeration for the different particle heating rates are predicted by the model of particle agglomeration, described by the equations (19) to (48). Figures 21 and 22 show the predictions of the volume fractions of unreacted coal C, liquid metaplast L, and coke-residue (char) E, the normalized contact area A, the surface tension force F_γ, the adhesive force due to coke interconnection F_E, and the adhesive force F_A as functions of time and particle heating rate of 10^4 K/sec and 10^5 K/sec, respectively. As indicated above (Section 5.1), these heating rates are representative of conditions in industrial combustors and laminar flow reactors. This approach is an alternative to that of separately calculating particle heating rates for different oxygen partial pressures, gas temperatures, and particle sizes. The two typical particle heating rates of 10^4 K/sec and 10^5 K/sec are chosen to show the effect of particle heating rate. Figure 23.a and 23.b correspond to the particle heating rate of 10^4 K/sec and 10^5 K/sec, respectively. As shown in these figures, the general trends of the curves of C, L, and E for the different particle heating rates are very similar,

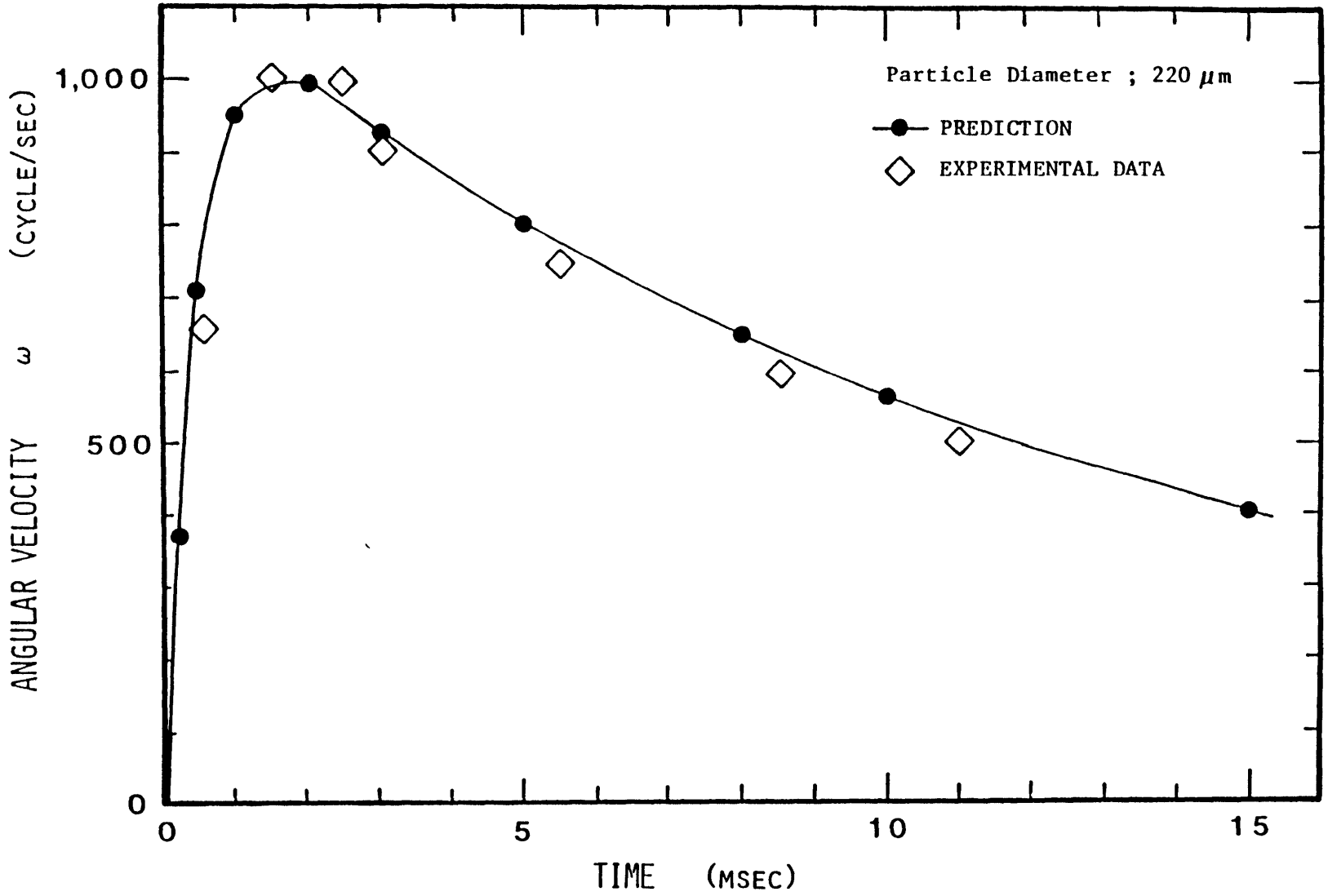

Figure 20. Comparison between Prediction and Experimental Data

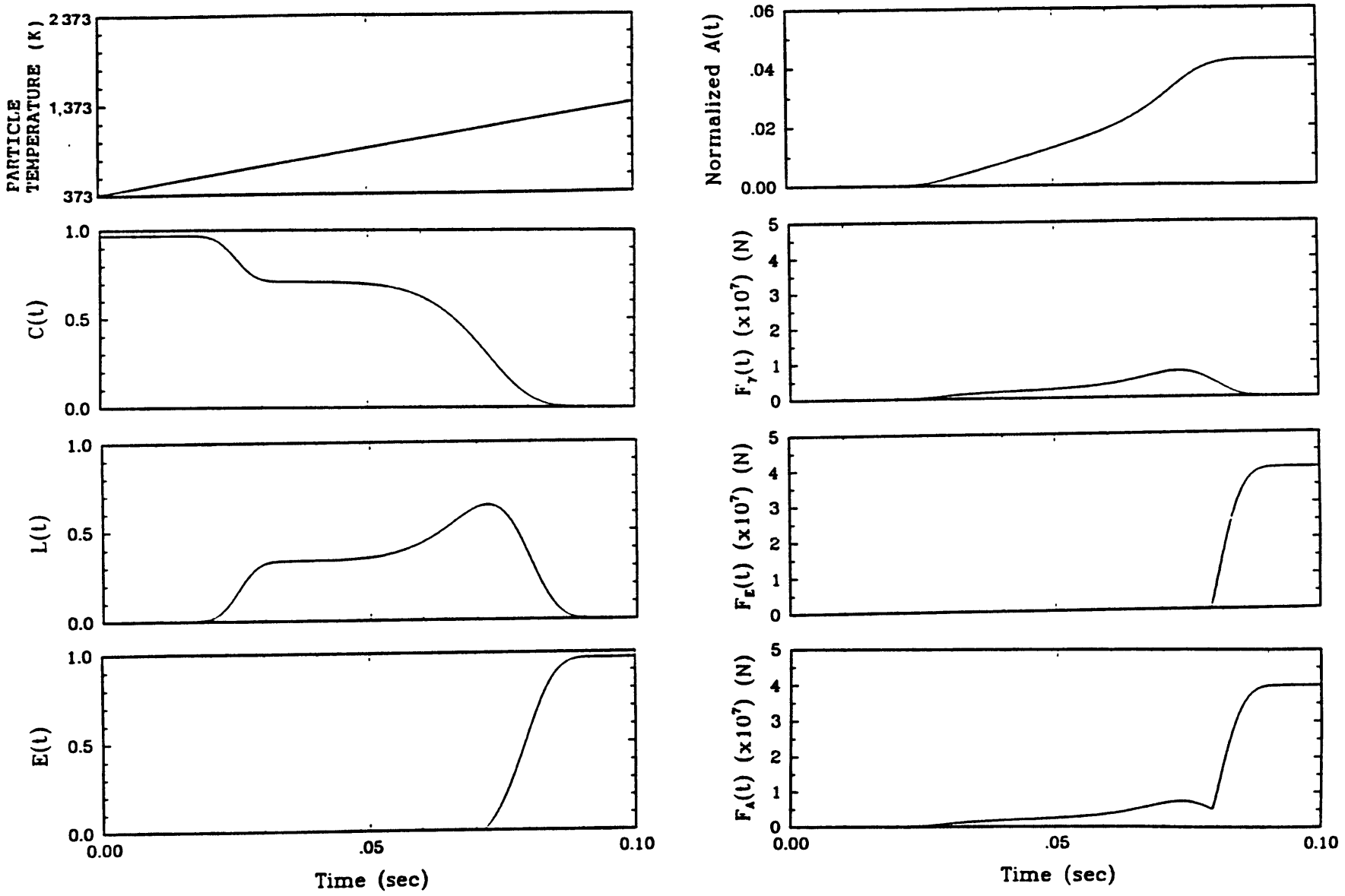

Figure 21. Predictions of C, L, E, Normalized A, F_γ, F_E, and F_A with Time for the Particle Heating Rate of 10^4 K/sec

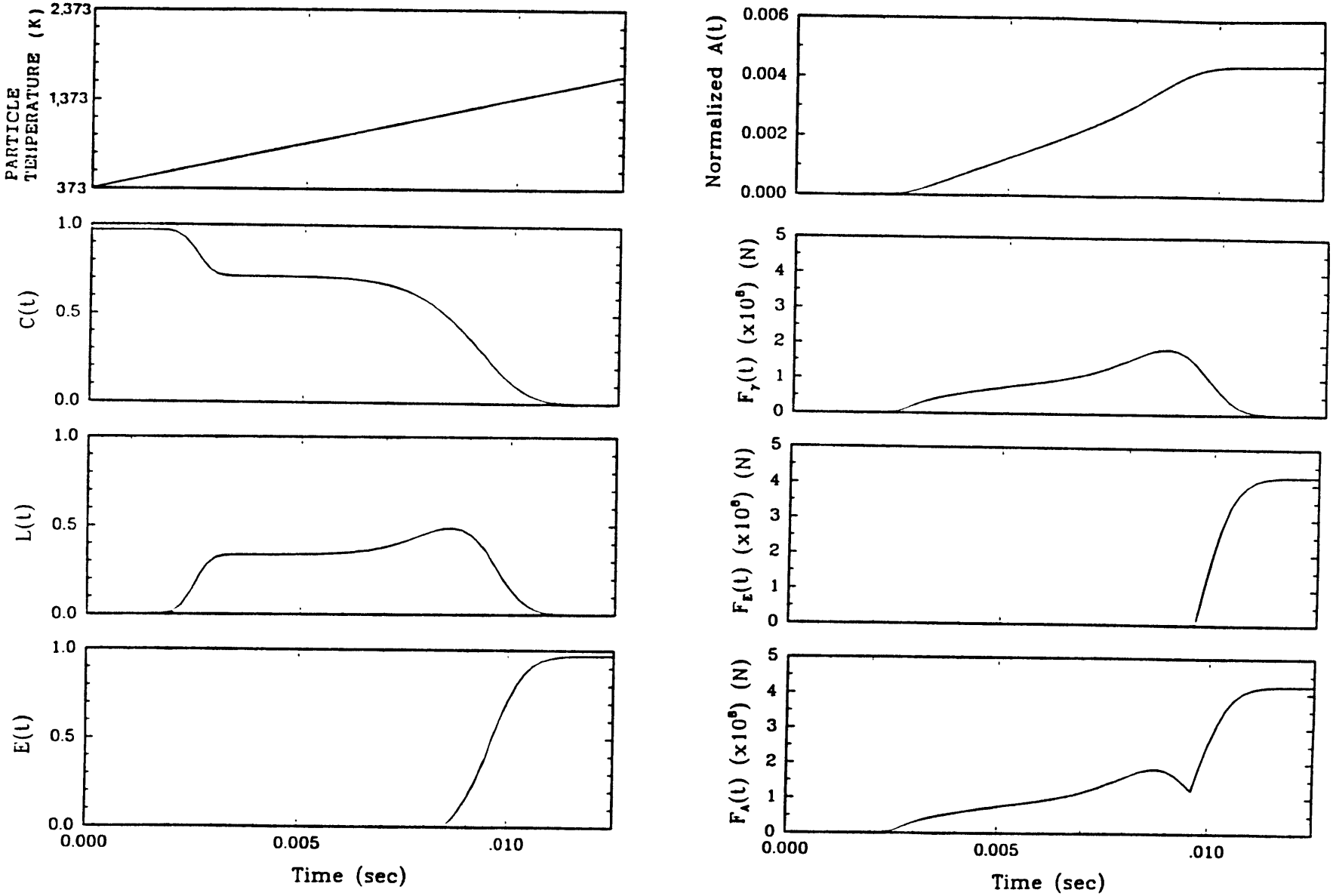

Figure 22. Predictions of C, L, E, Normalized A, F_Y, F_E, and F_A with Time for the Particle Heating Rate of 10^5 K/sec

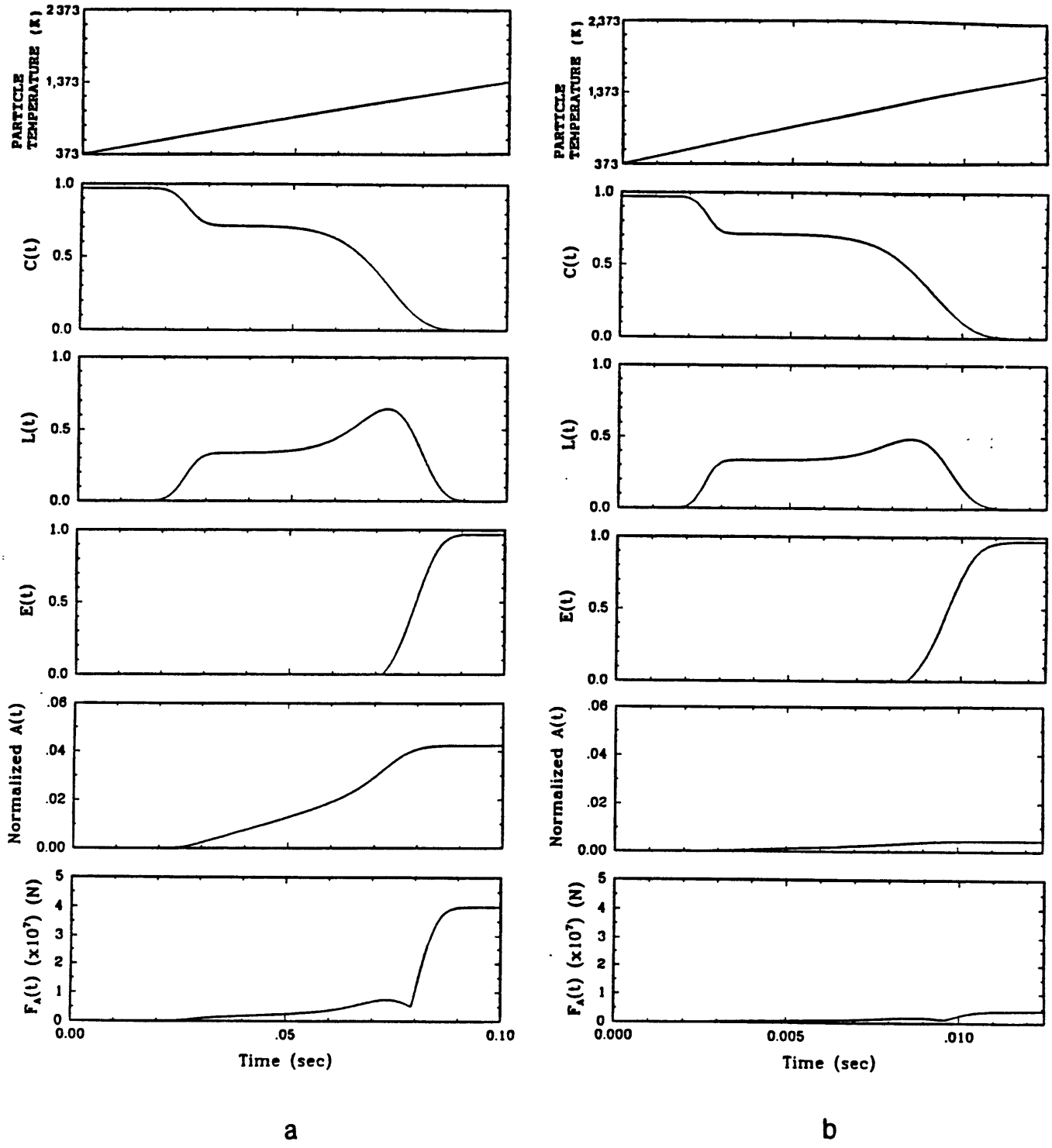

Figure 23. Comparisons of C, L, E, Normalized A, and Adhesive Force with Time for Different Particle Heating Rates (a) 10^4 K/sec (b) 10^5 K/sec

even though the time scales are totally different. The normalized contact area A, given by the contact area divided by the πx(Radius of Particle)^2, tends to decrease as the particle heating rate increases; this is due mainly to the decrease of the period in which the particles are plastic and in which any contact area growth must occur. Hence, the adhesive force, which is proportional to the contact area, tends to decrease as the particle heating rate increases. Consequently, it can be concluded that the higher particle heating rate reduces the tendency of coal particles to form agglomerates during particle heat-up, because it both decreases the strength of bonding of particles to each other and increases the centrifugal forces during devolatilization and char burnout.

CHAPTER 6. CONCLUSIONS

Coal particles in a CWF droplet can burn individually or as agglomerates depending upon combustion conditions. The present study provides tentative criteria for determining the importance of particle agglomerates during CWF droplet combustion.

The following conclusions are drawn from the experimental results and theoretical model predictions:

(1) The rotation and fragmentation of CWF particles, which have important ramifications on the space requirements for combustion and on the problems of erosion due to ash, are observed by high speed cinematography and two-color pyrometry.

(2) Particle rotation during devolatilization and char burnout generates centrifugal forces at the particle surface which can promote the separation of both weakly adhering char fragments and ash particles.

(3) The frequency of particle rotation is a strong function of the particle heating rate, which is directly influenced by oxygen partial pressure and gas temperature in a furnace.

(4) The adhesion force in the process of agglomeration of coal particles is strongly dependent upon the duration of plasticity of the particles.

(5) Rapid particle heating reduces the tendency of coal particles to form agglomerates during particle heat-up, because it both increases the centrifugal forces during devolatilization and decreases the strength of bonding of particles to each other. The models provide a basis for calculating the separation of char fragments and ash particles as a function of coal properties and the thermal history of coal particles.

APPENDIX

A.1. Spray Test Facility

A spray test facility to be used to characterize CWF spray is available in the 3 MW MIT Combustion Research Facility (CRF). A schematic of the Spray Test Facility (STF) is shown in Figure A.1.

Two sides of the 125 cm x 46 cm x 102 cm chamber have plexiglas walls for optical observation and measurement. About half of the other sides of the chamber have honeycomb sections through which air to be entrained by the spray can pass. The supply of outside air is necessary to suppress the recirculation of small particles into the path of the laser beam. Air at room temperature enters through the honeycomb sections when the exhaust fan is switched on. At exit from the spray chamber this entrained air and the atomizing air stream are separated from the CWF spray, and then flow through a filter and a flexible hose to the exhaust system of the CRF. The used CWF is collected in a storage tank through a pump.

A.2. Laser Diffraction Analyzer

The STF is equipped with a Laser Diffraction Spray Analyzer for droplet size measurements. The operational principle of the laser diffraction analyzer is based on the Fraunhofer diffraction pattern superimposed on the geometrical image, produced by droplets in the path of the monochromatic light beam. This analyzer manufactured by Malvern Instruments Inc., consists of a laser light source that passes light through the two plexiglas plates

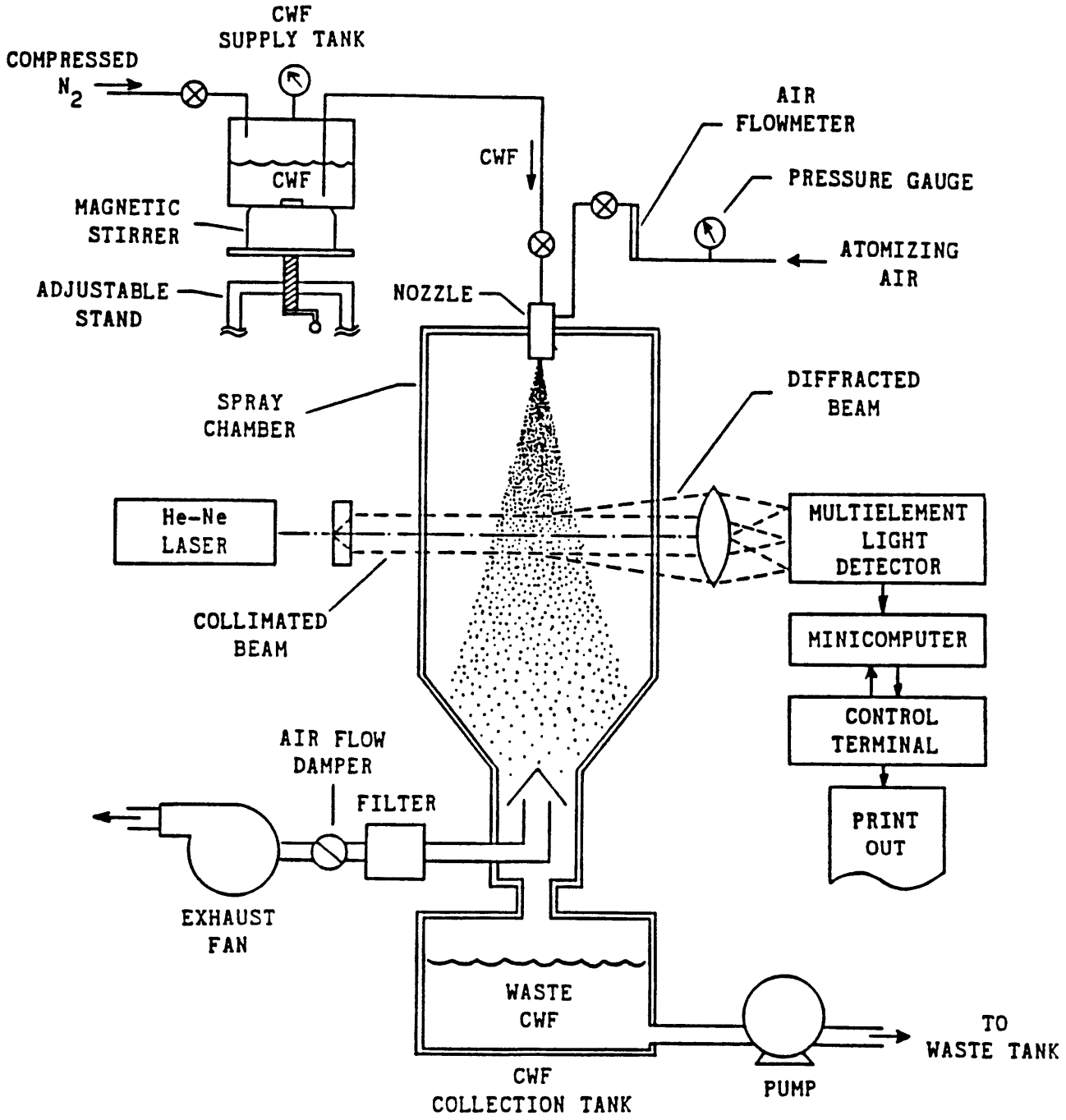

Figure A.1. Schematic Diagram of Spray Test Facility and Laser Diffraction Analyzer

perpendicular to the fuel spray flow, of a 30 multi-element photodetector that receives the light signal from the other side of the chamber, and of a minicomputer and a control terminal that process output signals from the photodetector to print out droplet size distributions or display on CRT. Figure A.1 shows a schematic diagram of the analyzer.

A computer program of the analyzer is capable of deducing the corresponding particle size distribution responsible for producing the measured light energy distribution in various functional forms, such as Normal, Log Normal, Rosin-Rammler or Model Independent. Six optical lenses are available for the analyzer. A focal length 63 mm lens will cover particle size 0.5 to 118 μm compared to a focal length 1000 mm lens for 19 to 1800 μm.

Additional information on the STF and the Laser Diffraction Spray Analyzer is available in Volume II, which is a companion to the present report.

A.3. Test Result of Atomizer

The atomizer has been tested in the Spray Test Facility which is equipped with the Laser Diffraction Spray Analyzer. ARC-fine grind CWF (69/31 coal/water by weight) was atomized and droplet sizes were measured. Air flowrate was varied from 40 liter/min to 70 liter/min, and CWF flowrate was varied from 30 g/min to 50 g/min. Figure A.2 shows a diagram of Mass Mean Diameter (MMD) of CWF versus air-to-fuel ratio (AFR). The air-to-fuel ratio was

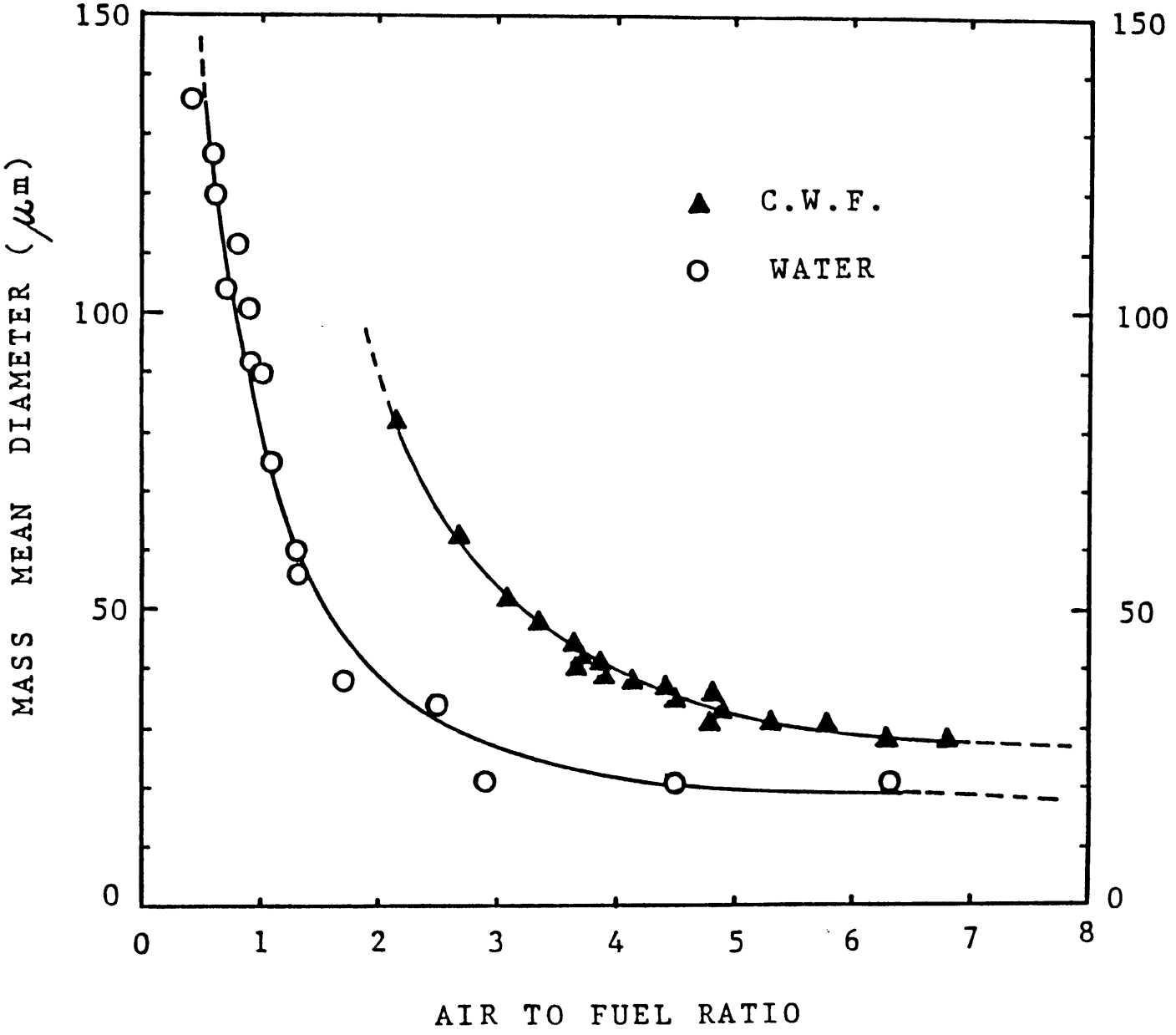

Figure A.2. Mass Mean Diameter of Spray Droplet at Various AFRs

varied from 0.4 to 7.0. Pure water was also tested for comparison. The smallest MMD of CWF droplets was found to be 28.0 μm, while that of water was 20.0 μm.

NOMENCLATURE

A	contact area
$\left(\frac{dA}{dt}\right)$	growth rate of contact area
A_i	exit area of devolatilization pore
ΣA_i	total exit area of devolatilization pores
A	area in eq (4)
cs	control surface
cv	control volume
$\tilde{C}$	mass fraction of unreacted coal
$\tilde{C}_i$	initial mass fraction of unreacted coal ($= 1-\tilde{f}_a$)
C	volume fraction of unreacted coal
$\tilde{E}$	mass fraction of coke-residue (char)
E	volume fraction of coke-residue (char)

E_{th} threshold volume fraction of coke-residue (char) $(\equiv \frac{1-\tilde{f}_a}{2})$

F_A adhesive force between two coalescent coal particles

$F_{centrif}$ centrifugal force acting on a coal particle

F_E adhesive force due to coke interconnection

F_{E1} adhesive force due to coke interconnection for stage 1

F_{E2} adhesive force due to coke interconnection for stage 2

F_{E3} adhesive force due to coke interconnection for stage 3

F_γ surface tension force due to liquid metaplast

$\tilde{f}_a$ mass fraction of ash (mineral matter)

f_a volume fraction of ash (mineral matter)

G	acceleration of gravity
k	devolatilization rate constant
k_I	rate constant in eq (19)
k_{II}	rate constant in eq (20)
$\tilde{L}$	mass fraction of liquid metaplast
L	volume fraction of liquid metaplast
L_S	total amount of solid metaplast initially existing in coal
ℓ_{eff}	effective circumference
M_O	original mass of CWF particle
m_C	mass of coal particle
R	radius of CWF particle
Re_r	rotational Reynolds number $(\equiv \frac{\rho r_p^2 \omega}{\mu})$
r	radial distance in eq (4)

r_c radius of coal particle

r_m rate of physical melting

r_p radius of CWF particle

r^* radius of contact area in neck region

T_F frictional drag

T_m mean melting temperature of coal particle

T_p temperature of CWF particle

t time

v volume in eq. (4)

V volatiles mass loss per unit original particle mass

V^* ultimate volatiles mass loss per unit original particle mass

$\frac{dV}{dt}$ rate of volatiles mass loss per unit original particle mass

v_e	exit velocity of volatiles at devolatilization pore
$\frac{\Sigma A_i \cos\theta_i \cos\phi_i}{\Sigma A_i}$	geometrical factor of devolatilization pores
Normalized A	normalized contact area, given by $\frac{A}{\pi r_c^2}$

Greek Symbols

γ_c	surface tension of melting coal particle
θ	contact angle
θ_i	angle
μ	viscosity
μ^*	viscosity of liquid metaplast
μ_{vol}	viscosity of volatiles
ρ_A	density of CWF particle in eq. (4)
ρ_a	density of ash (mineral matter)
ρ_c	density of unreacted coal
ρ_L	density of liquid metaplast
ρ_o	initial apparent density of CWF agglomerate
ρ_{vol}	density of volatiles
σ_E	bond stress of coke residue
σ_T	standard deviation of melting temperature of coal
ϕ_i	angle
ω	angular velocity of CWF particle

REFERENCES

1. Ehrlich, S., S. Drenker and R. Manfred, "Coal Use in Boilers Designed for Oil and Gas Firing," Proc. of the Am. Power Conf., Vol. 42, (1980).

2. Crouse, F., Combustion of Tomorrow's Fuels, Engineering Foundation Conference, Santa Barbara, CA, (November 1982).

3. Lapwood, K.J., P.J. Street, and F.D. Moles, "An Examination of the Behavior and Structure of Single Droplets of Coal-Oil Fuels During Combustion," pp. 924-944, Fifth Int. Symp. on Coal-Oil Mixture Combustion (1983).

4. Rah, S.C., Sc.D. Thesis, "Ignition and Combustion of Liquid Fuel Droplets; Impact on Pollutant Formation," Department of Chemical Engineering, M.I.T., Cambridge, MA., (January 1984).

5. Quann, R.J., M. Neville, M. Janghorbani, C.A. Mims, and A.F. Sarofim, "Mineral Matter and Trace-Element Vaporization in a Laboratory-Pulverized Coal Combustion System," Environ. Sci. Technol., Vol. 16, No. 11, pp. 776-781, (1982).

6. Timothy, L.D., A.F. Sarofim, and J.M. Beér, "Characteristics of Single Particle Coal Combustion," Nineteenth Symposium (International) on Combustion, The Combustion Institute, pp. 1123-1130, (1982).

7. Srinivasachar, S., S.W. Kang, L.D. Timothy, D. Froelich, A.F. Sarofim, and J.M. Beér, "Fundamentals of Coal-Water Fuel Combustion," Eighth International Symposium on Coal Slurry Fuels Preparation and Utilization, Orlando, FL (May 27-30, 1986).

8. Fong, W.S., Sc.D. Thesis," Plasticity and Agglomeration in Coal Pyrolysis," Department of Chemical Engineering, M.I.T., Cambridge, MA, (February 1986).

9. Holve, D.J., K. Gomi, and T.H. Fletcher, "Comparative Combustion Studies of Ultrafine Coal-Water Slurries and Pulverized Coal," The Seventh International Symposium on Coal Slurry Fuels Preparation and Utilization, New Orleans, LA (May 21-24, 1985).

10. Yu, T.U., S.W. Kang, M.A. Toqan, P.M. Walsh, J.D. Teare, J.M. Beér, and A.F. Sarofim, "Effect of Fuel Treatment on Coal-Water Fuel Combustion," Twenty-first Symposium (International) on Combustion, The Combustion Institute, Munich, W. Germany, (Aug. 1986).

11. Lamb, H., Hydrodynamics, 6th ed., Cambridge; Cambridge University Press, (1932).

12. Happel, J., H. Brenner, Low Reynolds Number Hydrodynamics, Noordhoff Int. Publish. Leyden, 2nd Ed., (1973).

13. Fitzgerald, D., "Kinetic Study of Coal Carbonization in the Plastic Zone," Fuel. Vol. 35, pp. 178, (1956).

14. Chermin, H.A.G., D.W. Van Krevelen, "Chemical Structure and Properties of Coal XVII - Mathematical Model of Coal Pyrolysis," Fuel. Vol. 36, pp. 85, (1957).

15. Fong, W.S., W.A. Peters, J.B. Howard, "Kinetics of Generation and Destruction of Pyridine Extractables in a Rapidly Pyrolyzing Bituminous Coal," Fuel, Vol. 65, pp. 251, (1986).

16. Frenkel, J., "Viscous Flow of Crystalline Bodies under the Action of Surface Tension," J. Phys. (USSR), Vol. 9, pp. 385, (1945).

17. Kingery, W.D., M. Berg, "Study of Initial Stages of Sintering Solids by Viscous Flow, Evaporation-Condensation, and Self-Diffusion," J. Appl. Phys., Vol. 26, pp. 1205, (1955).

18. Kuczynski, G.C., "Study of Sintering of Glass," J. Appl. Phys., Vol. 20, p. 1160, (1949).

19. Huang, D.D., "Flow Fields during Coalescence of Viscous Spheres," M.S. Thesis, Material Science and Engineering Department, M.I.T., (1976).

20. Frankel, N.A., and A. Acrivos, "On the Viscosity of a Concentrated Suspension of Solid Spheres," Chem. Eng. Sci., Vol. 22, pp. 847, (1967).

21. Nazem, F.F., "Rheology of Carbonaceous Mesophase Pitch," Fuel, Vol. 59, pp. 851, (1980).

22. Hwang, S.C., L. Tsonopoulos, J.R. Cunningham, G.W. Wilson, "Density, Viscosity, and Surface Tension of Coal Liquids at High Temperatures and Pressures," Ind. Eng. Chem. Proc. Des. Div., Vol. 21, pp. 127, (1982).

23. Taylor, G.H., "Development of Optical Properties of Coke during Carbonization," Fuel, Vol. 40, pp. 465, (1961).

24. Friel, J.J., S. Mehta, G.D. Mitchell, J.M. Karpinski, "Direct Observation of the Mesophase in Coal," Fuel, Vol. 59, p. 610, (1980).